Immune-like glycan-sensing and horizontally-acquired glycan-processing orchestrate host control in a microbial endosymbiosis

Benjamin H. Jenkins[1, 2]*, Estelle S. Kilias[1], Fiona R. Savory[1], Megan E. S. Sørensen[3,4], Camille Poirier[1], Victoria Attah[1], Georgia C. Drew[1], Luis J. Galindo[1], Guy Leonard[1], Duncan D. Cameron[3,5,6], Michael A. Brockhurst[3,7], David S. Milner[1] & Thomas A. Richards[1]*

[1]Department of Biology, University of Oxford, 11a Mansfield Road, Oxford OX1 3SZ, UK

[2]Department of Biochemistry, University of Cambridge, Tennis Court Road, Cambridge, CB2 1QW, UK

[3]Department of Animal and Plant Sciences, University of Sheffield, Sheffield S10 2TN, UK

[4]Institute of Microbial Cell Biology, Heinrich Heine University, 40225 Düsseldorf, Germany

[5]Department of Earth and Environmental Sciences, School of Natural Sciences, University of Manchester

[6]Manchester Institute of Biotechnology, University of Manchester, Manchester M1 7DN, UK

[7]Division of Evolution, Infection and Genomics, School of Biological Sciences, University of Manchester, Manchester M13 9PT, UK

Abstract

Endosymbiosis was a key factor in the evolution of eukaryotic cellular complexity. Yet the mechanisms that allow host regulation of intracellular symbionts, a pre-requisite for stable endosymbiosis and subsequent organelle evolution, are largely unknown. Here, we describe an immune-like glycan-sensing/processing network, partly assembled through horizontal gene-transfers (HGTs), that enables *Paramecium bursaria* to control its algal endosymbionts. Using phylogenetics, RNA-interference (RNAi), and metabolite exposure experiments, we show that *P. bursaria* regulates endosymbiont destruction using glycan-sensing/processing – a system that includes a eukaryotic-wide chitin-binding chitinase-like protein (*CLP*) localized to the host phago-lysosome. RNAi of *CLP* alters expression of eight glycan-processing genes, including two prokaryote-derived HGTs, during endosymbiont destruction. Furthermore, glycan-sensing/processing dynamically regulates endosymbiont number in *P. bursaria*, plasticity crucial to maximize host fitness across ecological conditions. *CLP* is homologous to a human phagocyte-associated innate immune factor, revealing how immune functions can be alternatively adapted and expanded, partly through HGT, enabling endosymbiotic control.

53 **Graphical Abstract**

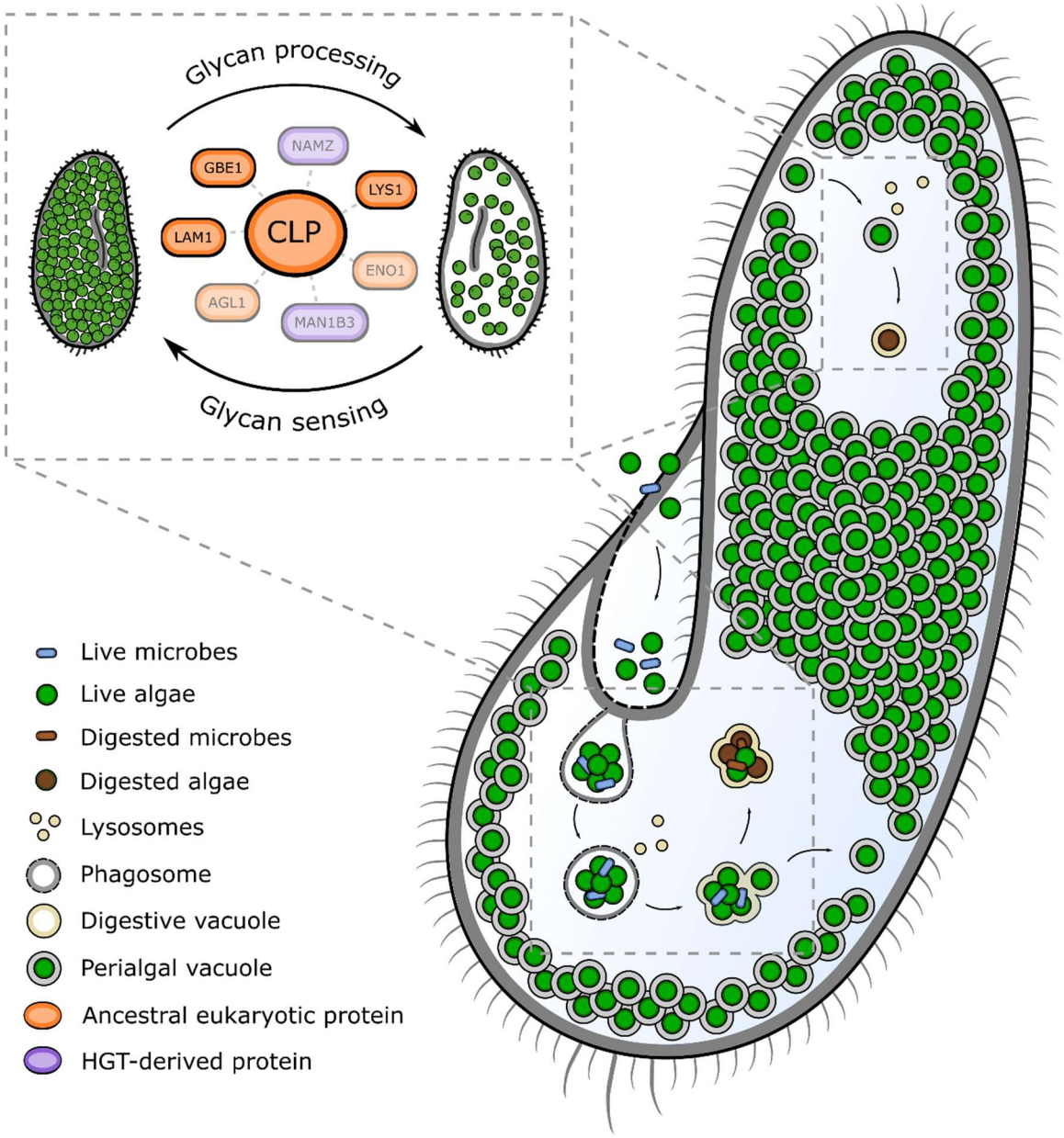

54

55

56

57

58

59

60

Main

Endosymbiosis played a crucial role in the evolution of eukaryotic cellular complexity[1–4] and underpins diverse ecologically and medically-significant host-microbe interactions (e.g., [5–11]). Long-term maintenance of a stable endosymbiosis requires a network of host mechanisms that regulate endosymbiont functions, allowing the host to maximize the fitness benefit of the interaction under fluctuating ecological conditions[12–15]. Orchestrating this network requires extensive genetic and cellular re-modelling by the host; however, the function and evolution of these mechanisms are poorly understood.

The ciliate protist, *Paramecium bursaria* (*Pb*), is an RNAi-tractable emerging model organism amenable for studying facultative endosymbiotic interactions[16–19]. Each cell maintains hundreds of intracellular green algae from the *Chlorella*-clade (e.g., *Chlorella* & *Micractinium*[20]) in a symbiosis involving photosynthesis-derived metabolite exchange[21–24]. Endosymbiotic algae are housed in modified host phagosomes (perialgal vacuoles) localized beneath the host cell cortex by microtubules[25–27]. *Pb* can regulate endosymbiont load through detachment and lysosomal fusion of the perialgal vacuole to trigger endosymbiont digestion[26–29]. In this manner, *Pb* dynamically controls the endosymbiont population in response to factors such as light intensity to maximize host fitness, often at the expense of individual endosymbiont fitness[13,29–31]. *Chlorella* algae possess cell walls composed of complex glycans (predominantly oligomannosides and chitin[32–34]) which a host must break-down to digest and thereby control its endosymbionts. Accordingly, the presence of *Chlorella* endosymbionts leads to increased expression of host chitin-processing genes in both *Pb*[35] and *Hydra viridis*[36], a metazoan host which also forms symbioses with *Chlorella* species[36].

Glycan processing and sensing requires functionally diverse glycosyl-hydrolases (GHs)[37,38]. GHs are widespread but discontinuously distributed in eukaryotes, with these enzymes performing important structural, nutritional and signaling functions in many ecologically-significant interactions[39–42]. This includes break-down and sensing of glycans derived from hosts, pathogens, other types of symbionts, or food[35,36,39,42–45]. Chitin oligosaccharides, such as the monosaccharide N-acetyl-glucosamine (GlcNAc), are common cues of innate immunity that can trigger both pathogen defense and symbiotic maintenance[42,44–48]. The spread of GHs in eukaryotes has been further facilitated by horizontal gene transfer (HGT), particularly among pathogens of glycan-producing hosts[49–56].

92 Here, we investigate the glycan-sensing and processing network in *Pb*, focusing on a
93 GlcNAc oligosaccharide binding chitinase-like protein (*CLP*) which is homologous to an innate
94 immune-factor protein in humans. We demonstrate using RNAi that host *CLP* perturbation
95 can disrupt endosymbiont destruction and alters the expression of intracellular signaling
96 systems and GH genes, suggesting a role in host sensing cascades and down-stream glycan-
97 processing. We demonstrate that 9 of the 37 GH genes in *Pb* (24%) were acquired via
98 prokaryote-to-eukaryote HGT, including two (a lysozyme – *NAMZ*; and a mannosidase –
99 MAN1B3) with altered expression during *CLP* RNAi perturbation, indicating how HGT can
100 augment ancestral functions of preexisting genes in order to facilitate a host-microbe
101 interaction. We show that RNAi perturbation of an additional GH gene (a eukaryotic lysozyme
102 – *LYS1*) also alters host control of endosymbiotic algae. We propose that a functional network
103 of immune-like glycan sensing, dependent upon *CLP*, and augmented by HGT-derived glycan
104 processing genes, has been repurposed as a mechanism of endosymbiont control in *Pb*
105 through the regulation of endosymbiont destruction. We discuss how such networks
106 represent a key innovation enabling hosts to regulate microbial endosymbionts.

107 **Results**

108 ***Horizontal gene-transfer has shaped glycan-processing in P. bursaria***

109 Host-microbe interactions are often governed by glycan-processing[44–48]. To identify the
110 repertoire of glycan-processing genes in *Pb* 186b[19], we designed a bioinformatic annotation
111 pipeline for the discovery of carbohydrate-active enzymes[37]
112 (https://github.com/benjaminhjenkins/CAZyme_survey). This identified a total of 37 putative
113 glycosyl-hydrolase (GH) (25 GH families; **Fig. S1a**) and 12 putative glycosyl-transferase (GT)
114 (10 GT families; **Fig. S1b**) encoding genes. Comparative analyses revealed a mosaic
115 distribution of GH and GT genes across the ciliates, including multiple instances of gene
116 duplication and loss (**Supplementary Dataset S1**).

117 Phylogenetic analyses were then conducted to identify candidate horizontal gene-
118 transfers (HGT) among the *Pb* GH genes. These resolved tree topologies for nine of the 37 *Pb*
119 GH genes (24.3%) that were best explained by HGT[57] from within the prokaryotes into a
120 eukaryotic ancestor lineage of *Pb*, given current genome sampling (**Fig. 1** – four HGT events
121 involving five *Pb* genes, discussed further below; see **Supplementary Table S1** and **Fig. S2** for

122 details on the additional four HGTs identified). Four of the putative HGT-derived genes were
123 shown to be acquired specifically in the *Pb* stem lineage (**Fig. 1a/c** & **S2 b/c**) and were present
124 in all five *Pb* strains assessed, ruling out genome project contamination. Comparison of
125 trimmed mean M (TMM) values of transcript abundance in *Pb* 186b[19] (under scramble control
126 RNAi conditions, see below) demonstrates transcription of each putative HGT-derived gene
127 with the exception of *MAN1B2*, indicating possible pseudogenization of *MAN1B2* following
128 *MAN1B1/2* gene duplication. Each putative HGT-derived gene contained introns
129 (**Supplementary Table S1**), including short introns characteristic of *Paramecia*[19].
130 Furthermore, each proposed open reading frame (ORF) contained between 9 and 43
131 UAG/UAA codons (representing 2.8% to 5.6% of codons per ORF; **Supplementary Table S1**),
132 which in *Paramecium*[58] code for glutamine rather than stop codons as translated in the
133 universal genetic code used by the prokaryotic progenitor lineage of the HGT. Collectively,
134 these data suggest that the putative HGT-derived genes have been integrated to function
135 within the host eukaryotic genome.

136 The proposed HGT-derived genes were annotated as encoding putative *β-*
137 *mannosidase* (*MAN1B1-3* and *MANEB*; **Fig. 1a** and **Fig. S2d**), *lysozyme* (*NAMZ* and *TTSA*; **Fig.**
138 **1b/c**), *β-glucosidase* (GAB; **Fig. S2a**), *cellulase* (CELA1; **Fig. S2b**), and *β-fructofuranosidase*
139 (INV; **Fig. S2c**) enzymes. Interestingly, the proposed functions of these HGT-derived genes are
140 enriched for cleavage of mannose (*MAN1B1-3*, *MANEB*) and GlcNAc (*NAMZ*, *TTSA*) containing
141 substrates – components of both bacterial food and the endosymbiotic algal cell wall[32–34] –
142 hinting that these HGT-acquired functions are important for mixotrophic functions and
143 endosymbiont control. These data reveal a mosaic distribution of glycan-processing genes in
144 *Pb* and the broader ciliate group that has been augmented by prokaryote-to-eukaryote HGT.

145 ***RNAi of a subset of glycan-processing genes perturbs host-mediated endosymbiont***
146 ***destruction, while perturbation of CLP determines expression of glycan-processing genes***

147 Next, we sought to understand whether *Pb* GH genes function in endosymbiont control. We
148 conducted an RNA-interference (RNAi) screen on *Pb* populations grown in microwell plates
149 and treated with cycloheximide to induce endosymbiont destruction[28,29]. Per-host
150 fluorescence (a proxy for endosymbiotic algal load[59]) was measured on an ImageXpress Pico
151 automated cell imaging system, and compared to 'non-hit' RNAi control (scramble)
152 populations to assess the effect of GH transcript perturbation on endosymbiont destruction

153 (**Fig. 2a**). RNAi of *u2af* –a splicing factor in *Pb* required for host growth– was used as a positive
154 RNAi control[16]. The RNAi screen was conducted twice (two biological replicates per treatment
155 with six technical replicate populations each; n = 12) and mean per-host fluorescence data
156 were assessed with a mixed effects model to account for uncontrolled sources of variance.
157 This revealed that 22% of observable variance could be attributed to RNAi-based gene
158 perturbation, 24% could be attributed to random effects (biological replicate and plate
159 positional artifacts), and 54% remained unexplained. Due to the high unexplained variability
160 and considerable influence of confounding factors, we have been conservative in our
161 interpretation of these data and consider the results set out below as trends.

162 RNAi of one GH and one GH family (chimeric RNAi-constructs were designed to target
163 multiple GH paralogues belonging to the same family; **Fig. S3**) led to higher per-host
164 fluorescence compared to scramble controls (control fluorescence = 44.6 relative
165 fluorescence units [RFU]) (**Fig 2a-b**), suggesting that perturbation of these genes stalls
166 endosymbiont destruction. These putative GHs were annotated as a *1,4-α-glucan branching*
167 *enzyme* (*GBE1*) proposed to function in glycogen biosynthesis (fluorescence = 49.3 RFU,
168 increased 10.6%; t=2.2, df=228, p=0.028) and a family of *lysosomal-α-mannosidases* (*LAM*)
169 predicted to cleave mannose (fluorescence = 49.3 RFU, increased 10.6%; t=2.2, df=272,
170 p=0.030). RNAi of two other GHs led to greater reduction in per-host fluorescence compared
171 to scramble controls (**Fig. 2a-b**), suggesting that perturbation of these genes may increase
172 endosymbiont destruction. These included a putative *chitinase-like protein* (*CLP*) predicted to
173 bind GlcNAc oligosaccharides (fluorescence = 38.3 RFU, reduced 14.2%; t=-3.1, df=291,
174 p=0.002) and a putative *Lys1-like lysozyme* (*LYS1*) predicted to cleave GlcNAc-GlcNAc (e.g.,
175 chitin) or GlcNAc-MurNAc (e.g., peptidoglycan) containing substrates (fluorescence = 41.0
176 RFU, reduced 8.1%; t=-1.97, df=290, p=0.050). The greater reduction in fluorescence observed
177 upon *CLP* RNAi is intriguing because an orthologue of this gene binds to glycan moieties such
178 as those present in *Chlorella* cell walls, and has been suggested to play a role in the sensing
179 of chitin-containing microbes, amongst other functions[60–62] (described in more detail below).
180 We hypothesize that CLP may act as a binding protein which functions in a glycan
181 processing/sensing signaling cascade involved in the regulation of endosymbiont load and
182 therefore sought to further explore the role of *CLP* during endosymbiont destruction in *Pb*.

183 If *CLP* functions in a signaling pathway which orchestrates endosymbiont control, *CLP*
184 RNAi perturbation should influence the transcription of other *Pb* encoded GH genes. To
185 explore whether GH function was altered during endosymbiont destruction in a *CLP*-
186 dependent manner, we assessed GH expression in cycloheximide treated and untreated
187 control cultures, and compared changes in expression under *CLP* RNAi or scramble control
188 RNAi conditions. Ensemble RNA sequencing was conducted under each condition and reads
189 were mapped to the *Pb* 186b genome[19]. To confirm *CLP* perturbation in response to RNAi,
190 reads were mapped only to the 3' *CLP* transcript end to avoid cross-talk from the *CLP* RNAi
191 construct (**Fig. 2c**). Importantly, *CLP* RNAi in untreated cultures resulted in 2.5-fold over-
192 expression of *CLP* (**Fig. 2d**), suggesting either that compensatory gene expression was
193 occurring in response to increased *CLP* dsRNA and subsequent siRNA exposure[16,63], and/or
194 that the RNAi signal (siRNA generation) had spread along the *CLP* transcript due to RNA-
195 dependent RNA-polymerase amplification of cleaved mRNA transcripts that are over-
196 represented in the mapped reads[16,64]. Both outcomes are known phenomena in *Paramecium*
197 RNAi experiments[16,63,64] and could interact, producing complexity in terms of phenotypic
198 outcome. Regardless, *CLP* RNAi resulted in significant perturbation in *CLP* transcript
199 abundance (**Fig. 2d**).

200 *CLP* RNAi during endosymbiont destruction significantly altered the expression of 8
201 (24%) GH genes (Bonferroni corrected since these did not test an *a priori* hypothesis; $p <$
202 0.0015) (**Fig. 2e**; **Fig. S4**). These include two putative GlcNAc-processing genes (*LYS1*; **Fig. 2a**,
203 and *NAMZ*; **Fig. 1b**) and two putative HGT-derived genes (aforementioned *NAMZ*, and
204 *MAN1B3*; **Fig. 1a**). The most significant changes in directionality of expression fold-change
205 during endosymbiont destruction, resulting from *CLP* RNAi, were observed for *LYS1*
206 (putatively involved in endosymbiont destruction; **Fig. 2a**), *MAN1B3* (a putative HGT-derived
207 gene predicted to cleave mannose; **Fig. 1b**), and *LAM1* (within a GH family putatively involved
208 in endosymbiont destruction; **Fig. 2a**). Interestingly, all three additional genes implicated in
209 endosymbiont control upon RNAi (*LYS1, GBE1* and *LAM1;* **Fig. 2a**) were significantly altered
210 upon *CLP* RNAi during endosymbiont destruction. These data demonstrate that a functional
211 network of glycan-processing genes, at least in part controlled by *CLP*, acts in the regulation
212 of endosymbiont destruction in *Pb*.

213 ***CLP RNAi alters expression of transcription factors and intracellular signaling systems***

214 To explore the broader role of *CLP* in *Pb*, we investigated how perturbed *CLP* function
215 influenced additional pathways triggered during endosymbiont destruction. Untargeted
216 metabolomics of *Pb* during *CLP* RNAi, compared to scramble control RNAi, revealed
217 enrichment in metabolites belonging to cell signaling (inositol phosphate, and
218 phosphatidylinositol signaling) and carbohydrate metabolic pathways (**Fig. 3a**; see also
219 **Supplementary Table S3**). A significant reduction in relative abundance of several metabolites
220 was detected upon *CLP* RNAi, including inositol 1,3,4-trisphosphate, fructose 1,6-
221 bisphosphate, and unspecified glucan disaccharides, which may include maltose, the product
222 of photosynthesis released by the algal endosymbionts[21–23] (**Fig. 3b**; **Fig. S5**).

223 We then assessed the expression of all *Pb* transcripts during endosymbiont
224 destruction (cycloheximide treatment) and *CLP* RNAi, compared to both untreated and
225 scramble control RNAi conditions (as per **Fig. 2e**). This identified distinct transcriptional
226 profiles for each condition (**Fig. 3c**), with clear separation observed between untreated and
227 cycloheximide treated cultures under scramble control RNAi conditions. A less distinct
228 separation profile was observed between untreated and cycloheximide treated cultures
229 during *CLP* RNAi, consistent with our hypothesis that functions associated with endosymbiont
230 destruction may be coordinated by *CLP*. To explore transcriptional patterns associated with
231 each treatment, we performed differential expression analysis for each pairwise condition.
232 Differentially expressed transcripts ([$\log_2$ fold change] ≥ 1, adjusted p-value < 0.001) were
233 hierarchically clustered based on relative expression under each condition (**Fig. 3d; Fig. S6**),
234 yielding three distinct transcript clusters (**Fig. 3e**; see also **Supplementary Table S4**).

235 Cluster 1 contains transcripts that are up-regulated during cycloheximide treatment,
236 independently of *CLP* RNAi (**Fig. 3f**), and includes genes related to autophagy (ser/thr-protein
237 kinase Atg1), intracellular destruction and transport (lipocalin, lipase), carbohydrate
238 metabolism (fructose-1,6-bisphosphatase; consistent with the mass spectrometry analysis,
239 **Fig. 3b**), and oxidative stress (glutathione peroxidase). We propose that these are genes
240 involved in the phago-lysosomal processes activated during destruction of algal
241 endosymbionts[25–29].

242 Cluster 2 contains transcripts predominantly down-regulated during cycloheximide
243 treatment in scramble control cultures (**Fig. 3g**), and so represent host functions possibly
244 inactivated during endosymbiont destruction. Interestingly, these transcriptional patterns

245 were not observed upon cycloheximide treatment coupled with *CLP* RNAi (**Fig. S6c-d**),
246 supporting the proposition that *CLP* RNAi can perturb endosymbiont control (seen in **Fig. 2a**).
247 This cluster includes genes predicted to function in signal transduction, and two putative
248 phosphatidylinositol binding proteins (again consistent with the metabolomics data; **Fig. 3a**)
249 indicating that phosphatidylinositol signaling is altered during regulation of endosymbiont
250 destruction. Phosphoinositides – a broad class of membrane phospholipids – are key
251 regulators of endosomal processes and downstream signals of extracellular receptor
252 activation, acting in intracellular membrane trafficking, autophagy, and innate immunity[65–69].
253 Other genes in this cluster were predicted to be involved in intracellular vesicular trafficking
254 (vacuolar sorting-associated proteins 9 & 12, and adaptin-like proteins) and cytoskeletal
255 arrangement (dynein heavy chain, and tubulin-tyrosine ligase/polyglutamylase). We propose
256 that these genes function in the cellular re-arrangements that maintain endosymbiosis in *Pb*,
257 and may represent processes that are inactivated during endosymbiont destruction, such as
258 detachment of the perialgal vacuole from the host cell cortex and lysosomal fusion[25–29]. The
259 observed down-regulation of these genes during algal destruction is consistent with the
260 proposal that these systems function in maintenance of the endosymbiotic population.

261 Cluster 3 contains transcripts with significantly increased expression during *CLP*
262 perturbation (**Fig. 3h**), irrespective of cycloheximide-induced endosymbiont destruction (as
263 in Clusters 1 and 2). This includes genes predicted to function in signal transduction, including
264 phosphatidylinositol signaling (as in **Fig. 3g**), serine-threonine protein kinases, transcription
265 factors, and a transcriptional activator. We therefore propose that these may be components
266 of a signaling cascade in which *CLP* is a component, and suggest that disruption of this signal
267 through *CLP* RNAi may be responsible for the increased endosymbiont destruction trend
268 observed during cycloheximide treatment (**Fig. 2a**). Taken together, these findings indicate
269 that complex signaling mechanisms are involved in host-mediated endosymbiont destruction,
270 and suggest that *CLP* may act as a key regulator of these molecular processes.

271 ***CLP localizes proximate to the putative host phagosome and lysosome during endosymbiont***
272 ***destruction***

273 To understand the role of *CLP* in endosymbiont regulation, we performed
274 immunofluorescence microscopy to track CLP localization during cycloheximide-induced
275 endosymbiont destruction. Using a custom polyclonal antibody raised against *Pb* CLP (see

276 **Methods**), we observed CLP localization to the host phagosome and oral apparatus (**Fig. 4a;**
277 see also **Supplementary Table S5**). These cell systems are part of the ciliate feeding grove[70,71]
278 and are associated with both heterotrophic feeding and establishment/regulation of
279 endosymbiotic algae[17,18]. A large fraction of the cells exhibited phagosome-like CLP
280 localization (78.4% of cells in untreated conditions, 85.7% in cycloheximide treated).
281 However, some cells demonstrated an additional pattern of CLP localization consistent with
282 host lysosomes (32.4% of cells in untreated conditions, 40.3% in cycloheximide treated; **Fig.**
283 **4b**). These observations indicate that *CLP* is involved in at least two systems (phagosomal and
284 lysosomal) which have complex overlapping functions. These data also demonstrate that the
285 sampled population includes cells which are at mixed stages of response, as identified by
286 differential CLP localization patterns. This result is consistent with host cell and associated
287 endosymbiotic functions not being synchronized (e.g., only 32.4% of cells demonstrating CLP-
288 lysosome localization and 78.4% of cells demonstrating CLP-phagosome localization under
289 standard conditions; **Supplementary Table S5**).

290 To explore how CLP localization is adjusted during endosymbiont destruction, we
291 compared algal autofluorescence and CLP immunofluorescence in *Pb* during cycloheximide-
292 induced endosymbiont destruction. A significant reduction in per-host algal fluorescence
293 during cycloheximide treatment (**Fig. 4c**) was coupled with increased CLP fluorescence (**Fig.**
294 **4d**). This trend was observed for both phagosome and phago-lysosome-like exhibiting cells,
295 indicating that endosymbiont destruction is coupled to *CLP* dynamics in both cellular
296 processes. These data support the hypothesis that *CLP* is functioning as a sensor for the
297 detection of endosymbiont or food-derived (**Fig. 4a-b**) glycan-substrates released during
298 endosymbiont destruction and heterotrophic feeding, and is consistent with data suggesting
299 the *LYS1* lysozyme (predicted to liberate these substrates and which is regulated by *CLP*) is
300 involved in endosymbiont destruction (**Fig. 3a, e**).

301 ***CLP is a chitin-binding protein homologous to an animal immune factor***

302 To further explore the function of *CLP* in *Pb,* we sought to understand the evolution of this
303 gene family across the eukaryotes. A single homologue of *Pb CLP*, *Stabilin-interacting*
304 *Chitinase-like Protein* (*SI-CLP*), was identified in the human genome. *SI-CLP* is an innate
305 immune-factor expressed in macrophages and neutrophils that activates signal-cascades
306 involved in inflammatory responses[62] (including phosphoinositide kinases[72]; **Fig. 3a**, **f-h**), and

307 is sorted into CD63+/LAMP1-positive lysosomes and p62lck-positive late endosomes in
308 mammals, indicating a role in secretory, digestive and autophagy-related intracellular
309 trafficking[61]. *SI-CLP* has broad substrate-binding capacity that includes GlcNAc
310 oligosaccharides and other glycan moieties, and may play a sensory role in host responses to
311 chitin-containing pathogens[60]. No homologue for the *stabilin-1* protein, with which human *SI-*
312 *CLP* interacts, was identified in *Pb* or other ciliates (NCBI protein database; gathering
313 threshold: e-01; June 2024) and so this protein was not explored further.

314 Phylogenetic reconstruction of 1,445 candidate homologues reveals that *CLP* is
315 present in the majority of extant eukaryotic phyla searched (**Supplementary Dataset S2**)
316 demonstrating that this is an anciently-derived eukaryotic gene family. An amino acid
317 alignment of representative eukaryotic *CLP* homologues (**Fig. 5a**; **Fig. S7**) revealed strong
318 conservation of binding sites (all but one retained in 90% of the homologues aligned) and
319 predicts the presence of a 5' secretion signal peptide sequence in 75% of the sequences
320 sampled (DeepLoc2.0)[73]. Identifiable chitin cleavage sites[60,61] were not conserved, with
321 universal absence of the 2nd and 4th known catalytic residues, and 78% of species compared
322 lacking all but one known catalytic residue. Putative binding and cleavage sites were mapped
323 to the predicted structure of *Pb* CLP (AlphaFold3; May 2024) revealing a pore-like structure in
324 which GlcNAc oligosaccharide binding is proposed to occur (**Fig. 5b**). Comparison with the
325 crystal structure of *H. sapiens (Hs)* SI-CLP[60] (which forms a dimer; **Fig. S8**) reveals positional
326 similarity of binding and cleavage sites. Western blot analysis of *Pb* CLP reveals two bands
327 close to 37 kDa and 75 kDa (predicted molecular weight of *Pb* CLP, 40.24 kDa; see **Fig. S9**)
328 indicating that the *Pb* homologue may also form a dimer.

329 *Pb CLP* and *Hs SI-CLP* lack the conserved 'DxxDxDxE' motif associated with chitin-
330 cleavage (**Fig. 5c**). To understand catalytic function, *Pb* CLP engineered to carry a
331 *Saccharomyces* secretion peptide was expressed in a chitinase-deficient *Saccharomyces*
332 *cerevisiae* strain, and the secretome assayed using a Chitinase Activity Kit (**Fig. 5d**). We
333 observed low catalytic activity of *Pb* CLP on all substrates compared to *Pb* HEXB (predicted to
334 cleave terminal GlcNAc residues from glycan chains; **Fig. 2b**). It is important to note that low
335 activity of all enzymes, including HEXB, may be due to the required assay conditions (37°C)
336 being sub-optimal for *Pb* enzymes (~18-25°C). Nonetheless, we observed that directed
337 mutation of the 2nd and 4th active site residues of *Pb CLP* (*CLPΔ;* **Fig. 5c**) 'restored' cleavage

338 function and significantly increased activity on 2mer ($GlcNAc_2$ / $Chitin_2$) (t=3.141; df=6;
339 p=0.020) and 3mer ($GlcNAc_3$ / $Chitin_3$) (t=3.324; df=6; p=0.021) substrates (**Fig. 5d**),
340 supporting the hypothesis that these residues are important for catalytic activity. These data
341 indicate that *CLP* is a eukaryotic wide gene family which functions in GlcNAc oligosaccharide
342 (e.g., chitin) binding, but lacks potent cleavage activity, supporting our hypothesis that *CLP*
343 plays a role in glycan sensing.

344 ***Glycan break-down products alter host control of endosymbiotic algae***

345 Our genomic and RNAi data point to glycan-sensing/processing being central to host-
346 mediated endosymbiont control. As such, we next explored how glycan break-down
347 substrates were altered during regulation of endosymbiosis in *Pb*, and the reciprocal effect of
348 these substrates on endosymbiont control. Here, we used altered light intensity to trigger
349 endosymbiont destruction[13,30] to simulate conditions experienced by *Pb* in nature. We
350 observed a reduction in *Pb* per-host fluorescence upon exposure to high-light (80 μ mol m^{-2} s^{-}
351 ^{1}; **Fig. 6a**). This was accompanied by no comparable reduction in host cell number (**Fig. 6b**)
352 indicating that these conditions did not have a negative effect on host viability during the
353 period of the experiment. Analysis of metabolite abundance in *Pb* under varying light
354 conditions (50 μ mol m^{-2} s^{-1} to 6 μ mol m^{-2} s^{-1})[30] revealed that reduction in endosymbiont load
355 was accompanied by increased abundance of GlcNAc and glucosamine (GlcN – a substrate
356 which also binds to *SI-CLP*[60]) (**Fig. 6c**; **Fig. S10**). These substrates are consistent with break-
357 down products of chitin-like glycans[32–34] (**Fig. 6d**) and support the hypothesis that host control
358 of endosymbiotic *Chlorella*[13,30] is facilitated through break-down of glycans present in the
359 algal cell wall. This is also consistent with the predicted function and involvement of *LYS1* (**Fig.
360 2a/e**) and the HGT-derived *NAMZ* (**Fig. 2e**) in endosymbiont destruction under *CLP*-derived
361 transcriptional control.

362 Given the putative role of *CLP* as a glycan-sensor, we next tested how increased glycan
363 abundance influenced endosymbiont control in *Pb*. We observed increased per-host
364 fluorescence upon exposure to chitin, GlcNAc, and GlcN under standard growth conditions
365 (**Fig. 6e**). This effect was greatest upon exposure to GlcNAc and remained significant at lower
366 doses (0.1 mM; t=4.314; df=20; p=1.34^{-04}), indicating sensitivity to this substrate which
367 determined symbiotic outcomes. Supplementing separately cultured endosymbiosis-derived
368 algae with GlcNAc did not enable heterotrophic growth or improve autotrophic growth

369 compared to nitrogen free conditions (**Fig. S11a/b**), demonstrating that the response to
370 chitin, GlcNAc, and GlcN seen in host was not due primarily to an algal growth response. Host
371 exposure to chitin oligomers (t=18.860-24.805; df=50; $p < 2e^{-6}$), GlcNAc (t=12.896; df=50; $p <$
372 $2e^{-6}$), N-acetyl-d-glucosamine-6-phosphate (GlcNAc-6P) (t=3.922; df=50; p=0.004), and GlcN
373 (t=3.5; df=50; p=0.010) during high-light treatment all significantly arrested the reduction in
374 per-host fluorescence associated with endosymbiont destruction (**Fig. 6f**). Exposures were
375 conducted at equal molar concentrations indicating that the length of the chitin polymer
376 chain may be an important factor. No response was observed for D-glucosamine-6-phosphate
377 (GlcN-6P) or glucose (Glc), indicating that this effect was not due to increased nutrient
378 provision (carbon, nitrogen, or phosphate) to the host. Importantly, these GlcNAc mono- and
379 oligosaccharides are consistent with substrates bound by *CLP* (**Fig. 5d**), and putative products
380 of GlcNAc-processing GHs (e.g., *LYS1*) implicated in *CLP*-dependent endosymbiont destruction
381 (**Fig. 2a/e**).

382 Finally, we sought to explore how broader mixotrophic functions could influence
383 endosymbiont control. *Pb* is a mixotroph and phagocytoses bacteria in nature, therefore the
384 host must be exposed to additional sources of glycans. We observed that exposure to heat-
385 killed gram-positive bacteria, possessing exposed peptidoglycan-rich cell walls, also increased
386 algal fluorescence per-host (t=4.492; df=75 ; p=$2.51e^{-05}$) compared to heat-killed gram-
387 negative bacteria delivered at the same dose (**Fig. 6g**; **Fig. S12**). This suggests that broader
388 microbial trophic interactions, including mixotrophic feeding, may also influence the
389 dynamics of endosymbiosis in *Pb.*

390 These data have revealed that exposure to GlcNAc, and other break-down products of
391 glycans present in endosymbiotic algae and the cell walls of bacterial food, can alter
392 endosymbiont control in *Pb.* We propose that *CLP*, which functions to bind these substrates,
393 may act to regulate the broader cellular network that underpins this process. We therefore
394 postulate that glycan-sensing and processing represents an important mechanism of
395 endosymbiont control in *Pb* through the regulation of endosymbiont destruction.

396 **Discussion**

397 Here we show that an immune-like glycan-sensing/processing network involving a conserved
398 eukaryotic chitinase-like protein (*CLP*), and augmented by genes acquired through HGT,

399 orchestrates the regulation of endosymbiosis in *Pb*. We demonstrate that host-mediated
400 destruction of endosymbiotic algae releases glycan-substrates (**Fig. 6c**), specifically GlcNAc
401 and GlcN, and that environmental exposure to GlcNAc mono- and oligosaccharides stalls
402 endosymbiont destruction (**Fig. 6f**). Through comparative phylogenetics we reveal that *CLP* is
403 related to an innate immune-factor in humans (*SI-CLP*) involved in phago-lysosomal response
404 pathways and possible molecular-sensing of pathogens[60–62], and show that *CLP* in *Pb* serves a
405 similar function to coordinate phago-lysosomal activity. *CLP* localizes to the oral apparatus,
406 phagosome, and lysosome of *Pb* with increasing localization intensity during endosymbiont
407 destruction (**Fig. 4d**), where GlcNAc-substrates arise as they are liberated through
408 endosymbiont destruction (**Fig. 6c**) or bacterial feeding (**Fig. 6g**). We propose that these
409 substrates are acted upon by at least six ancient eukaryotic genes (e.g., *LYS1* - a GH that
410 directly determines the fate of algal endosymbionts*;* **Fig. 2a**) and two horizontally-acquired
411 glycan-processing genes (e.g., *MAN1B1, NAMZ;* **Fig. 1b**) which are transcriptionally regulated
412 by *CLP* function (**Fig. 2e**). We hypothesize that this mechanism of glycan-sensing through *CLP*
413 triggers a network of cellular processes involving transcriptional regulation, intracellular
414 signaling (**Fig. 3f**-**h**) and glycan-processing (**Fig. 2e**) to regulate endosymbiont destruction in
415 *Pb*.

416 Intriguingly, this host network of cellular processes includes genes acquired by *Pb*
417 through prokaryote-to-eukaryote HGT. Among the genes altered through *CLP* perturbation
418 during endosymbiont destruction are two genes proposed to be HGT-derived. *MAN1B3* (**Fig.**
419 **2a**), a predicted β-mannosidase, may be important for destruction of mannose-substrates in
420 the endosymbiont cell wall. However, *NAMZ* (**Fig. 2b**), a predicted lysozyme, is potentially the
421 most relevant, as this enzyme is proposed to cleave GlcNAc in chitin (i.e., from the
422 endosymbionts cell wall) or peptidoglycan (i.e., from the bacterial cell wall) substrates. The
423 interaction of predicted cleavage products of HGT-derived *NAMZ* (i.e., GlcNAc) with *CLP* (**Fig.**
424 **5d**) and their effect on endosymbiont destruction dynamics in the host (**Fig. 6e, f**), combined
425 with the finding that *CLP* perturbation influences subsequent expression of *NAMZ* (**Fig. 2e**),
426 suggests that this may represent part of the feedback loop of glycan-processing and sensing
427 proposed to occur during endosymbiont destruction. These observations demonstrate how
428 recently acquired gene functions (e.g., *NAMZ*) following HGT can augment ancestral functions
429 (*CLP*).

430 'You are what you eat' is a hypothesis which posits that phagocytosis can drive HGT,
431 from consumed cells to host nuclei, through establishment of a gene-transfer ratchet[74]. This
432 process has been posited as an important factor in endosymbiotic organelle acquisition during
433 eukaryotic evolution. The 'shopping bag' model went further, stating that the step-wise
434 acquisition of genes from former, phagocytosed cells (i.e., food), sometimes involving cells
435 which formed transient endosymbioses, built the host genetic repertoire required for
436 endosymbiotic functions that, in turn, allows for stable symbiont integration[75,76]. This process
437 is thought to be key for the evolution of plastid (chloroplast) organelles (i.e., eukaryotic
438 photosymbiosis). In *Pb*, we observe data consistent with both hypotheses relating to the
439 function of a facultative endosymbiosis, but with a fundamental addition. Here, the genes
440 acquired by *Pb* arose not from transient interactions with eukaryotic algae, but from bacteria.
441 The occurrence of bacterial genes in eukaryotic genomes is not uncommon[54], though few
442 cases have been reported in ciliates[77–80] but also involve the transfer of GH genes, supporting
443 the idea that genes that function in glycan-processing are prime candidates for prokaryote-
444 to-ciliate HGT. *Paramecium* are well known for their ability to phagocytose or form stable
445 symbiotic interactions with a diverse consortium of bacterial species[81–84]. Thus, we
446 hypothesize that these genes likely originated from ancestral bacteria maintained either
447 stably or transiently in endosymbiosis[85,86], or ingested as food[74,76]. Regardless, our discovery
448 that these genes of bacterial origin may be involved in endosymbiotic algal destruction in *Pb*
449 illuminates how cross-kingdom HGT can shape host-microbe endosymbiotic interactions
450 consistent with both the 'you are what you eat' and the 'shopping bag' hypotheses.

451 The role of innate immunity in plant-microbe and animal-microbe symbioses is well-
452 understood[44,46,47,87], however such mechanisms have yet to be described in a single-celled
453 endosymbiotic system[88,89]. *Pb* lacks many components of a 'canonical' immune system
454 (**Supplementary Table S6**). Yet detection of self from non-self must be critical to allow the
455 host to defend against harmful microbial pathogens[90–92], and mechanisms of molecular
456 sensing that can determine friend from foe, or 'good' symbionts from 'bad', are essential for
457 a host maintaining a population of intracellular symbionts[5,7,12–15,87,93]. This is important when
458 the fitness interests of symbiont and host are not aligned, resulting in conflict between
459 partners – an inevitability in symbiosis[94]– and whereby detection and resolution of conflict
460 are needed for long-term stability of an interaction[13,29,31,95]. In *Pb*, maintenance of a

461 population of endosymbiotic algae requires significant re-modelling and co-opting of host
462 cellular machinery[18,25–27]. As such, a finely tuned network of molecular processes is required
463 that allows the host to detect context-dependent cues, and respond to, initiate, maintain, or
464 terminate the interaction. Here, we propose that this process occurs through the sensing of
465 glycan-substrates released during endosymbiont destruction or microbial feeding (**Fig. 6a-f**),
466 detected by *CLP*, and subsequent signaling that prompts the host to stall further
467 endosymbiont destruction. This process would act to minimize the costly effects of mass
468 endosymbiont destruction[29], perpetuating surviving endosymbionts, and promoting long-
469 term stability of the interaction. Our discovery highlights how a putatively ancient mechanism
470 of immune-like glycan sensing, shaped partly by functions acquired via prokaryote-to-
471 eukaryote HGT, can be co-opted for control of a facultative endosymbiotic interaction. We
472 propose that this functional network of glycan processing and sensing represents an
473 important factor in how stable host-microbe associations have evolved.

474 **Data Availability**

475 All data and script used for analysis and processing are available at:
476 https://github.com/benjaminhjenkins/Paramecium_bursaria. All sequence reads are
477 available on NCBI GenBank with the BioProject identifier PRJNA65904 and SRA accession
478 number SRR1251101, and at: https://github.com/guyleonard/paramecium and
479 https://zenodo.org/doi/10.5281/zenodo.4638887.

480 **Acknowledgements**

481 This work was primarily supported by an ERC Consolidator Grant (CELL-in-CELL), Gordon and
482 Betty Moore Foundation (GBMF) grant (GMBF11490) and a Royal Society University Research
483 Fellowship (UF130382) to T.A.R.. MAB and DDC were supported by grants from the BBSRC
484 (BB/X016439/1) and NERC (NE/V000128/1). We thank Prof. Neil Gow of the University of
485 Exeter for informative discussions on chitin sensing which inspired this work. The authors
486 gratefully acknowledge the Micron Advanced Bioimaging Facility (supported by Wellcome
487 Strategic Awards 091911/B/10/Z and 107457/Z/15/Z) for their support & assistance in this
488 work.

489 **Declaration of interests**

490 The authors declare no competing interests

491 **Methods**

492 ***Culture conditions and media***

493 In all experiments, *Paramecium bursaria* (*Pb*) 186b (CCAP 1660/18) strain was used. *Pb* cells
494 were cultured in New Cereal Leaf – Prescott Liquid media (NCL), unless modified as described.
495 NCL media was prepared by adding 4.3 mgL^{-1} $CaCl_2.2H_2O$, 1.6 mgL^{-1} KCl, 5.1 mgL^{-1} K_2HPO_4, 2.8
496 mgL^{-1} $MgSO_4.7H_2O$ to deionised water. 1 gL^{-1} wheat bran was added, and the solution boiled
497 for 5 minutes. Once cooled, media was filtered once through Whatman Grade 1 filter paper
498 and then through Whatman GF/C glass microfiber filter paper. Filtered NCL media was
499 autoclaved at 121°C for 30 mins to sterilise prior to use.

500 NCL medium was bacterized with *Klebsiella pneumoniae* SMC and supplemented with
501 0.8 mgL^{-1} β-sitosterol prior to propagation. *Pb* 186b cells were sub-cultured 1:9 into fresh
502 bacterized NCL media every two months and maintained at 23°C at a light intensity of 25 = µ
503 mol m^{-2} s^{-1} (standard – e.g., **Fig. 6a/b**) or 80 µ mol m^{-2} s^{-1} (high – e.g., **Fig. 6a/b**) with a light-
504 dark (LD) cycle of 12:12 h. *Pb* cultures were maintained for at least three weeks following sub-
505 culture to ensure that cells were starved and in stationary phase prior to experimentation.

506 In free-living algal assays, *Micractinium conductrix* SAG 241.80 (a member of the
507 *Chlorella* clade[20,22]) was used, as axenic algal endosymbionts isolated from *Pb* 186b could not
508 be reliably cultured. This strain was isolated from *Pb* SAG 27.96 and shares an identical ITS2
509 sequence with the *M. conductrix* endosymbiont of *Pb* 186b[96]. Algae were cultured in Modified
510 Bold's Basal Medium (MBBM) medium at 24°C with a 14:10 h LD cycle.

511 For bacterial feeding assays the following strains were used: *Escherichia coli* HT115
512 (Ec); *Klebsiella pneumoniae* SMC (Kp); *Serratia marascens* BS303 (Sm); *Leucobacter celer*
513 *subsp. astrifaciens* CBX151T (Ls); *Actinetobacter baumanii* (Ab); *Bacillus subtilis* 168 (Bs);
514 *Psuedomonas aeruginosa* PA14 (Pa); *Enterococcus faecalis* OG1RF (Ef); *Staphylococcus aureus*
515 MSSA476 (Sa); *Citrobacter freundii* (Cf); *Bifidobacterium breve* (Bb); and *Lactobacillus ruminis*
516 (Lr). Bacteria were cultured overnight (constant shaking, 30°C) in Luria-Bertani broth (Ec – Pa)
517 or Todd-Hewitt (Ef – Sa) broth based on standard cultivation methods, or in modified Gifu

518 Anaerobic Medium (mGAM; Nissui Pharmaceuticals) (Cf – Lr) under anaerobic conditions[97]
519 (5% H2, 5% CO2, 90% N2, <20 ppm O2).

520 For yeast secretion assays, *Saccharomyces cerevisiae* Y16947 (Euroscarf) was used.
521 This strain is a *S. cerevisiae* BY4742 CTSI deletion mutant (YLR286cΔ). *S. cerevisiae* was
522 cultured in YPD at 30°C and stored at -80°C in 25% glycerol solution.

523 ***Phylogenetic analysis***

524 Dataset generation and sampling for each phylogenetic analysis were conducted as follows.
525 For identification of CAZymes in *Pb*, predicted proteins[19] were searched with a custom
526 annotation tool (https://github.com/benjaminhjenkins/CAZyme_survey). For HGT analysis,
527 dataset curation was conducted as described by Irwin et al.[98]. Briefly, datasets consisting of
528 representative eukaryote proteins from all available major eukaryotic supergroups, and viral
529 proteins excluding over-represented Human Immuno-deficiency Virus-1, were clustered into
530 protein families using Diamond BLASTp and Markov Clustering. Hidden-Markov models
531 (HMMs) of clustered protein families were used to search a dataset of prokaryote proteins,
532 limited to 150-bacterial top hits per genus, and the resulting eukaryote, viral, and prokaryote
533 protein families were merged and re-clustered. For a full overview of HGT dataset curation,
534 including software versions and settings used, see Irwin et al.[98]. For a phylogeny of *CLP* in
535 eukaryotes, *Pb* 186b *CLP* and *Homo sapiens* (*Hs*) *SI-CLP* sequences were used to conduct
536 clade-specific searches of the NCBI protein database (gathering threshold: e-01, December
537 2023), including all available major eukaryotic supergroups and avoiding over-representation
538 from metazoan and plant taxa. These were added to an *SI-CLP* orthologue dataset (OrthoDB)
539 to give a final dataset of 1,445 candidate homologous amino acid sequences.

540 For all datasets, protein sequences were aligned using MAFFT v7.508[99] and masked
541 using TrimAL v1.4.15[100] allowing for no gaps. Each alignment was manually inspected, and
542 highly divergent or identical sequence paralogs from the same genomic source were manually
543 removed. Phylogenies were generated using IQ-TREE v2.2.0.3[101] with 1,000 ultra-fast
544 bootstraps. Models for each tree were calculated using IQ-TREE's ModelFinder
545 implementation according to Bayesian inference criterion (BIC) and are detailed in the
546 relevant figure legends. Bootstrap methods and models chosen for tree generation are listed
547 in the respective figure legends.

548 ***RNAi feeding***

549 A full protocol for RNAi feeding and imaging in *Pb* is available at:
550 dx.doi.org/10.17504/protocols.io.8epv5jzm4l1b/v1. Briefly, *Pb* was fed with *E. coli*
551 transformed with an L4440 plasmid construct with paired IPTG-inducible T7 promoters,
552 facilitating targeted gene perturbation through the phagotrophic delivery of complementary
553 double-stranded (ds)RNA. L4440 plasmid constructs (**Supplementary Table S7**) were
554 transformed into *E. coli* HT115 competent cells and grown overnight on LB agar (50 μgmL^{-1}
555 Ampicillin and 12.5 μgmL^{-1} Tetracycline) at 37°C. Positive transformants were picked and
556 grown overnight in LB (50 μgmL^{-1} Ampicillin and 12.5 μgmL^{-1} Tetracycline) at 37°C with shaking
557 (180 rpm). Overnight pre-cultures were back-diluted 1:25 into 15 mL of LB (50 μgmL^{-1}
558 Ampicillin and 12.5 μgmL^{-1} Tetracycline) and incubated for a further 2 hours under the same
559 conditions, until an OD_{600} of between 0.4 and 0.6 was reached. *E. coli* cultures were then
560 supplemented with 0.4 mM IPTG to induce template expression within the L4440 plasmid,
561 and incubated for a further 3 hours under the same conditions. *E. coli* cells were pelleted by
562 centrifugation (3100 x *g* for 2 mins), washed with sterile NCL media, and pelleted once more.
563 *E. coli* cells were then re-suspended in NCL media supplemented with 0.4 mM IPTG, 100 μgmL^{-}
564 ^{1} Ampicillin, and 0.8 μgmL^{-1} β-sitosterol, 2% glycerol, and adjusted to a final OD_{600} of 3. *E. coli*
565 cells were split into single-use aliquots and stored at -20°C until feeding[102].

566 *Pb* cells were pelleted by gentle centrifugation in a 96-well plate (10 mins at 800 x *g*),
567 taking care not to disturb the cell pellet by leaving 100 µL of supernatant, and re-suspended
568 2:5 into 150 µL of diluted, induced *E. coli* culture media (to make 250 µL total; final OD 0.1).
569 Feeding was conducted daily for 6 days using frozen bacterial stocks and, where
570 cycloheximide was added alongside feeding, this was added on days 4 and 5 to a final
571 concentration of 50 μgmL^{-1}. The orientation of construct position on the microwell plates was
572 altered between experiments, ensuring different columns and rows were used for each
573 construct between experiments (see analysis below).

574 ***Live cell imaging***

575 High-throughput imaging was performed on an ImageXpress Pico Automated Cell Imaging
576 System (Molecular Devices) at 4x magnification, using the Cy5 (absorbance: 630/40 nm;
577 emission: 695/45 nm) channel to capture algal-chlorophyll autofluorescence as described

578 previously[29]. Images were automatically stitched together using the built-in
579 CellReporterXpress image acquisition software, generating a composite tiled image for each
580 well for downstream analysis. Individual cells in each well were masked using the
581 MetaExpress software and the average fluorescence of each object scored. Data for RNAi
582 screening (**Fig. 2a**) and glycan substrate / bacterial feeding (**Fig. 6a, e-g**) experiments were
583 gated by shape [0.6 < shape factor < 0.9], size [area < 10,000] and fluorescence [average
584 fluorescence intensity < 150] to select for single intact *Pb* cells during cycloheximide
585 treatment.

586 Average per-host fluorescence data for RNAi screening experiments (Fig. 2a) were
587 analysed using a linear mixed effects model using the lme4[103] and lmerTest[104] packages. The
588 model included separate random intercepts accounting for row position, column position,
589 and experimental block to control for batch and/or positional artefacts during imaging.
590 Degrees of freedom to calculate p-values were estimated using the Satterthwaite
591 approximation. Average per-host fluorescence data for glycan substrate / bacterial feeding
592 (**Fig. 6a, e-g**) experiments were analysed using a linear model on log-transformed data (**Fig.**
593 **6a, e-g**). All analyses were performed using R version 4.2.1.

594 ***RNA sequencing and differential expression analysis***

595 *Pb* cultures (6x replicates) were subject to RNAi feeding (as above) for 6 days prior to
596 harvesting, including a penultimate 2 days of cycloheximide treatment for the corresponding
597 samples. *Pb* cells (~50,000 per sample) were strained three times through a 40 µm cell strainer
598 to remove large debris, collected on an 11 µm filter, washed with NCL, and resuspended into
599 1 mL of TriZol reagent. RNA was extracted using the Zymoprep RNA extraction kit and stored
600 in nuclease-free water at -20°C. RNA was processed using the Illumina NovaSeq 6000 v1.5
601 workflow (Illumina™) with polyA selection. A 150 bp paired-end library was prepared and
602 resulted in 1,184,917,880 reads total consisting of 177,737,682,000 bp (SRA accession:
603 SRR1251101).

604 Paired-end reads were trimmed to remove adapters and primers using the TrimGalore
605 v0.6.7-1 wrapper tool of Cutadapt[105]. Trimmed reads were then aligned to our *Pb* 186b Pacbio
606 genome assembly[19] using BOWTIE2 v2.5.1[106], and contamination filtered using Samtools
607 v1.7[107] to keep only host *Pb* mapped sequences (80-90% of all reads). Normalized transcript

608 expression values for each read data set were calculated and cross-sample normalization
609 performed using Salmon v1.10.2[108]. Differential expression analysis was conducted using
610 DESeq2 v1.34.0[109] to assess change in relative transcript abundance between pairwise data
611 sets.

612 For four-way analysis of gene expression, pb186bvf_008968-T1 (corresponding to *Pb*
613 *CLP*) and 11 transcripts (with highly variable or over 75% zero read counts) were removed
614 prior to differential expression analysis to aid in downstream clustering of less differentially
615 expressed transcripts. These sequences were retained in each pair-wise analysis of gene
616 expression. For pairwise and four-way analysis of gene expression, differentially expressed
617 transcripts (|log2 fold change| ≥ 0.5, adjusted p-value < 0.001) were clustered based on
618 normalized read counts. Hierarchical clustering was performed using Pearson correlation and
619 a maximum height cut-off of 80%. Transcript annotation was conducted by manual curation
620 of differentially expressed transcripts using InterProScan.

621 ***Mass spectrometry***

622 For metabolomics following *CLP* RNAi, *Pb* cultures (6x replicates) were subject to RNAi feeding
623 (as above) for 7 days prior to harvesting. *Pb* cells (~40,000 per sample) were filtered onto 11
624 µm nylon filters (Merck Millipore NY1104700) to minimise residual bacteria. The cells were
625 washed with water, and the cells resuspended from the filter in 500 µL 80% v/v HPLC-grade
626 methanol. The samples were transferred to 1.5 mL microcentrifuge tubes, snap frozen in
627 liquid nitrogen, and stored at -80°C. Samples were subjected to LC/MS analysis using a
628 derivatised C18 method by the metabolomics facility at the University of Oxford, Department
629 of Chemistry. Data were subjected to sample-specific normalisation based on manual cell
630 counts, followed by median normalisation, log transformation, and Pareto scaling using
631 MetaboAnalyst v5.0[110] (https://genap.metaboanalyst.ca/). Data were then analysed using a
632 one-way ANOVA, followed by a Fisher's Least Significant Difference test with false discovery
633 rate (FDR) adjusted p-values (based on the Benjamini–Hochberg procedure[111]).

634 For metabolomics of *Pb* 186b under differential symbiont load, cultures were first
635 grown at 50 µ mol m^{-2} s^{-1} to increase cell densities, and then split and acclimated to their
636 treatment conditions of low (6 µ mol m^{-2} s^{-1}) or moderate-high (50 µ mol m^{-2} s^{-1}) light intensity
637 for 3 days. They were then sampled and analyzed as described previously[24]. Briefly, *Pb* cells

638 were filtered on 11 µm nylon filters, washed in Volvic water, and then the cells were disrupted
639 by sonication (20% power for 10 s). The *Pb* fraction was collected by pushing 1 mL of the lysate
640 through a 1.6 µm filter, which caught the intact endosymbiont cells. The samples were
641 analyzed with a Synapt G2-Si with Acquity UPLC, recording in positive mode over a large
642 untargeted mass range (50 – 1000 Da). A 2.1x50mm Acuity UPLC BEH C18 column was used
643 with acetonitrile as the solvent. Masses of interest were investigated using the MarVis-Suite
644 2.0 software[112] (http://marvis.gobics.de/), using retention time and mass to compare against
645 KEGG[113] (https://www.genome.jp/kegg/) and MetaCyc[114] (https://biocyc.org/) databases.

646 ***Immunofluorescence microscopy and Western Blot of the Pb CLP proteins***

647 *Pb* cells were prepared for immunofluorescence microscopy using the protocol available at:
648 dx.doi.org/10.17504/protocols.io.yxmvm2ozng3p/v1. Primary rabbit polyclonal antibodies
649 for CLP were generated by Thermo Fisher Scientific, using the peptide sequence detailed in
650 **Supplementary Table S7**. Imaging was performed on a ScanR Olympus with a 20X objective
651 (refraction index = 1; emission = 698 [chlorophyll], 515 [Alexa Fluor 488]). Images were
652 collected using cellSens Dimension Software v3.2 and analysed using FIJI ImageJ2 version
653 2.3.0[115]. In brief, background noise was removed from the z-stack images using the 'rolling
654 ball background subtraction' (r=15). To count and analyse the fluorescence of the algae, a
655 smoothing gaussian blur filter was applied, and the z-stacks were combined to create a 2D
656 image. To resolve any overlapping cells, a Watershed segmentation was used after
657 thresholding the image with Otsu method. Processed images were false-coloured to aid
658 visualisation. Cells were manually scored based on whether they exhibited phagosome-like
659 fluorescence (localized to the oral groove and early endosome), lysosome-like fluorescence
660 (localized to small lysosome-like structures clustered around endosymbiotic algae), or both
661 (**Supplementary Table S5**). Algal fluorescence per-host cell and maximum *CLP* fluorescence
662 per host-cell were analysed using a linear model (**Fig. 4c/d**).

663 For Western Blot, *Pb* cells were first cleaned from debris by straining the culture
664 through a 40 µm cell strainer and washing the cells with autoclaved NCL media. The cells were
665 collected and concentrated via centrifugation (800 x *g* for 10min). Proteins were extracted for
666 30 min in 2x SDS buffer (55°C) supplemented with a mixture of protease-inhibitor (Roche;
667 Cat.4693116001), 2 µl of RNAse A (Qiagen; Cat. 19101) and 2 µl DNAse I (Fisher Scientific;
668 Cat. EN0521). The detailed protocol for the Western Blot of *Pb* is available at:

669 dx.doi.org/10.17504/protocols.io.ewov1q58kgr2/v1. Imaging was performed on an
670 iBrightCL1000 imager.

671 ***Yeast heterologous expression of Pb putative chitin interacting proteins***

672 *S. cerevisiae* Y16947 was transformed with a p426 GPD plasmid (ATCC 87361) containing a
673 gene expression insert modified with a 5' mating factor α (MFA) signal peptide sequence, or
674 an empty p426 GPD plasmid control, as described previously[49].

675 Transformants were grown for 7 days on SCM-URA at 30°C with shaking at 180 rpm,
676 then centrifuged at 3,200 x *g* for 5 mins and the supernatant collected. Supernatant from
677 each culture was centrifuged at 3,200 x *g* for 40 mins using a Spin-X UF concentrator 10,000
678 MWCO (Corning) to collect proteins over 10 kDa. Collected protein was washed in PBS and
679 matched to a concentration of 120 µg/mL prior to use. Protein activity assays were conducted
680 using 10 µL of sample (3x replication) on a Chitinase Activity Kit (Sigma-Aldrich #CS0980)
681 following the manufacturer's instructions, with incubation at 37°C for 3 hours. Comparisons
682 of catalytic function were analyzed using a generalized linear model with quasi-binomial
683 distribution (**Fig. 5d**).

684 ***Symbiont load assessment using flow cytometry***

685 *Pb* cultures to assess symbiont load in **Fig. 6c** and **Fig. S10** were grown under varying light
686 conditions (0, 6, 12, 24 and 50 µ mol m^{-2} s^{-1}) with a light-dark (LD) cycle of 14:10 h for seven
687 days. Symbiont load was estimated using a CytoFLEX S flow cytometer (Beckman Coulter Inc.,
688 CA, USA) by measuring the intensity of chlorophyll fluorescence for single *Pb* cells (excitation
689 488nm, emission 690/50nm) and gating cell size using forward side scatter[59].

690 ***Glycan substrate and bacterial feeding***

691 *Pb* cultures were washed twice with NCL and filtered using a 40 µm cell strainer to remove
692 large debris prior to feeding. For substrate feeding, *Pb* cells (~150 in 300 µL) in a 96-well plate
693 were supplemented with 0.01 mM, 0.1 mM, or 1 mM of glycan substrate in NCL media
694 (**Supplementary Table S8**). Concentrations of each substrate used are stated in the respective
695 figure panels. *Pb* cultures (6x replicates) were maintained under normal growth conditions at
696 either standard (25 µ mol m^{-2} s^{-1}) or high (80 µ mol m^{-2} s^{-1}) light intensity for up to 72 hours
697 prior to imaging.

698 For bacterial feeding, bacterial stocks were grown overnight for 48 hours, washed
699 twice in NCL, and fed to *Pb* cells (~75-100 in 250 µL) at a final OD_{600} of 0.1. *Pb* cultures (6x
700 replicates) were maintained under normal growth conditions for up to 48 hours prior to
701 imaging (see below).

702 ***Algal growth assays***

703 To determine if *M. conductrix* SAG 241.80 can utilize GlcNAc as a carbon source for
704 heterotrophic growth, growth assays were performed in continuous darkness over a 7-day
705 period in BBM+V media (CCAP) supplemented with 1 mM L-arginine using Biolog Phenotype
706 MicroArrays™ PM1 plates. Populations (3x replication) were initiated at a density of
707 approximately 5 x 106 cells/ml and changes in optical density (OD740) were regularly
708 recorded. Heterotrophic growth on GlcNAc was compared with negative (no carbon source)
709 and positive (α-D-glucose control treatments).

710 To determine if *M. conductrix* SAG 241.80 can utilize GlcNAc as a nitrogen source, growth
711 assays with 1 mM GlcNAc supplementation were performed over a 10-day period and
712 changes in optical density (OD740) were compared with negative (no nitrogen, -N) and
713 positive control (1 mM L-arginine supplementation) treatments. The algae were nitrogen
714 starved in BBM+V media (CCAP) lacking a nitrogen source (i.e., BBM+V-N) for 24 hours before
715 the growth assays commenced. Populations (6x replication) were then initiated in 96 well
716 plates at a density of approximately 5 x 106 cells/ml in BBM+V containing 100 mM MES and
717 100 mM MOPS buffer and, where applicable, 1 mM of the nitrogen source to be tested at pH
718 5.5, 6.5 and 7.5. Plates were incubated at 24°C with a 14/10 h LD cycle for 10 days and OD740
719 readings were regularly recorded.

720 **REFERENCES**

721 1. Bonen, L., Cunningham, R. S., Gray, M. W. & Doolittle, W. F. Wheat embryo mitochondrial 18S
722 ribosomal RNA: evidence for its prokaryotic nature. *Nucleic Acids Res* **4**, 663–671 (1977).
723 2. Bonen, L. & Doolittle, W. F. On the prokaryotic nature of red algal chloroplasts. *Proc Natl Acad*
724 *Sci U S A* **72**, 2310–2314 (1975).
725 3. Archibald, J. M. The puzzle of plastid evolution. *Curr Biol* **19**, R81-8 (2009).

726 4. Keeling, P. J. The number, speed, and impact of plastid endosymbioses in eukaryotic evolution.
727 *Annual Review of Plant Biology* **64**, 583–607 (2013).
728 5. McFall-Ngai, M. J. & Ruby, E. G. Symbiont recognition and subsequent morphogenesis as early
729 events in an animal-bacterial mutualism. *Science* **254**, 1491–1494 (1991).
730 6. McFadden, G. I., Reith, M. E., Munholland, J. & Lang-Unnasch, N. Plastid in human parasites.
731 *Nature* **381**, 482–482 (1996).
732 7. Baker, A. C. Flexibility and specificity in coral-algal symbiosis: Diversity, ecology, and
733 biogeography of *Symbiodinium*. *Annu. Rev. Ecol. Evol. Syst.* **34**, 661–689 (2003).
734 8. Curtis, B. A. *et al.* Algal genomes reveal evolutionary mosaicism and the fate of nucleomorphs.
735 *Nature* **492**, 59–65 (2012).
736 9. Husnik, F. *et al.* Horizontal gene transfer from diverse bacteria to an insect genome enables a
737 tripartite nested mealybug symbiosis. *Cell* **153**, 1567–1578 (2013).
738 10. Werner, G. D. A., Cornwell, W. K., Sprent, J. I., Kattge, J. & Kiers, E. T. A single evolutionary
739 innovation drives the deep evolution of symbiotic N2-fixation in angiosperms. *Nat Commun* **5**,
740 4087 (2014).
741 11. Kwong, W. K., Del Campo, J., Mathur, V., Vermeij, M. J. A. & Keeling, P. J. A widespread coral-
742 infecting apicomplexan with chlorophyll biosynthesis genes. *Nature* **568**, 103–107 (2019).
743 12. Kiers, E. T., Rousseau, R. A., West, S. A. & Denison, R. F. Host sanctions and the legume–
744 rhizobium mutualism. *Nature* **425**, 78–81 (2003).
745 13. Lowe, C. D., Minter, E. J., Cameron, D. D. & Brockhurst, M. A. Shining a light on exploitative
746 host control in a photosynthetic endosymbiosis. *Curr Biol* **26**, 207–211 (2016).
747 14. Foster, K. R., Schluter, J., Coyte, K. Z. & Rakoff-Nahoum, S. The evolution of the host
748 microbiome as an ecosystem on a leash. *Nature* **548**, 43–51 (2017).
749 15. López-Madrigal, S. & Duarte, E. H. Titer regulation in arthropod-*Wolbachia* symbioses. *FEMS*
750 *Microbiol Lett* **366**, fnz232 (2019).

751 16. Jenkins, B. H. *et al.* Characterization of the RNA-interference pathway as a tool for reverse
752 genetic analysis in the nascent phototrophic endosymbiosis, *Paramecium bursaria*. *R. Soc. open*
753 *sci.* **8**, rsos.210140, 210140 (2021).
754 17. Fujishima, M. & Kodama, Y. Mechanisms for establishing primary and secondary
755 endosymbiosis in *Paramecium*. *Journal of Eukaryotic Microbiology* **69**, e12901 (2022).
756 18. Jenkins, B. H. Mutualism on the edge: Understanding the *Paramecium–Chlorella* symbiosis.
757 *PLOS Biology* **22**, e3002563 (2024).
758 19. Leonard, G. *et al.* De novo genome sequence assembly of the RNAi-tractable endosymbiosis
759 model system *Paramecium bursaria* 186b reveals factors shaping intron repertoire.
760 2024.08.09.607295 Preprint at https://doi.org/10.1101/2024.08.09.607295 (2024).
761 20. Hoshina, R., Iwataki, M. & Imamura, N. *Chlorella variabilis* and *Micractinium reisseri* sp. nov.
762 (Chlorellaceae, Trebouxiophyceae): Redescription of the endosymbiotic green algae of
763 *Paramecium bursaria* (Peniculia, Oligohymenophorea) in the 120th year. *Phycological Research*
764 **58**, 188–201 (2010).
765 21. Ziesenisz, E., Reisser, W. & Wiessner, W. Evidence of de novo synthesis of maltose excreted by
766 the endosymbiotic *Chlorella* from *Paramecium bursaria*. *Planta* **153**, 481–485 (1981).
767 22. Arriola, M. B. *et al.* Genome sequences of *Chlorella sorokiniana* UTEX 1602 and *Micractinium*
768 *conductrix* SAG 241.80: implications to maltose excretion by a green alga. *The Plant Journal* **93**,
769 566–586 (2018).
770 23. Kato, Y. & Imamura, N. Effect of sugars on amino acid transport by symbiotic *Chlorella*. *Plant*
771 *Physiol Biochem* **46**, 911–7 (2008).
772 24. Sørensen, M. E. S. *et al.* Comparison of independent evolutionary origins reveals both
773 convergence and divergence in the metabolic mechanisms of symbiosis. *Current Biology* **30**,
774 328-334.e4 (2020).
775 25. Nishihara, N. *et al.* Microtubule-dependent movement of symbiotic algae and granules in
776 *Paramecium bursaria*. *Cell Motil Cytoskeleton* **43**, 85–98 (1999).

777 26. Takahashi, T., Shirai, Y., Kosaka, T. & Hosoya, H. Arrest of cytoplasmic streaming induces algal
778 proliferation in green paramecia. *PLoS ONE* **2**, e1352 (2007).
779 27. Kodama, Y. & Fujishima, M. Synchronous induction of detachment and reattachment of
780 symbiotic *Chlorella* spp. from the cell cortex of the host *Paramecium bursaria*. *Protist* **164**,
781 660–672 (2013).
782 28. Kodama, Y. & Fujishima, M. Cycloheximide induces synchronous swelling of perialgal vacuoles
783 enclosing symbiotic *Chlorella vulgaris* and digestion of the algae in the ciliate *Paramecium*
784 *bursaria*. *Protist* **159**, 483–94 (2008).
785 29. Jenkins, B. H. *et al.* Emergent RNA–RNA interactions can promote stability in a facultative
786 phototrophic endosymbiosis. *PNAS* **118**, (2021).
787 30. Sørensen, M. E. S., Wood, A. J., Cameron, D. D. & Brockhurst, M. A. Rapid compensatory
788 evolution can rescue low fitness symbioses following partner switching. *Current Biology* **31**,
789 3721-3728.e4 (2021).
790 31. Horas, E. L., Metzger, S. M., Platzer, B., Kelly, J. B. & Becks, L. Context-dependent costs and
791 benefits of endosymbiotic interactions in a ciliate–algae system. *Environmental Microbiology*
792 **24**, 5924–5935 (2022).
793 32. Gerken, H., Donohoe, B. & Knoshaug, E. Enzymatic cell wall degradation of *Chlorella vulgaris*
794 and other microalgae for biofuels production. *Planta* **237**, (2012).
795 33. Higuchi, R., Song, C., Hoshina, R. & Suzaki, T. Endosymbiosis-related changes in ultrastructure
796 and chemical composition of *Chlorella variabilis* (Archaeplastida, Chlorophyta) cell wall in
797 *Paramecium bursaria* (Ciliophora, Oligohymenophorea). *European Journal of Protistology* **66**,
798 149–155 (2018).
799 34. Hiramatsu, S., Ishihara, M., Fujie, M., Usami, S. & Yamada, T. Expression of a chitinase gene and
800 lysis of the host cell wall during *Chlorella virus* CVK2 infection. *Virology* **260**, 308–315 (1999).
801 35. Kodama, Y. *et al.* Comparison of gene expression of *Paramecium bursaria* with and without
802 *Chlorella variabilis* symbionts. *BMC Genomics* **15**, 183 (2014).

803 36. Hamada, M. *et al.* Metabolic co-dependence drives the evolutionarily ancient *Hydra–Chlorella*
804 symbiosis. *eLife* **7**, e35122 (2018).
805 37. Lombard, V., Golaconda Ramulu, H., Drula, E., Coutinho, P. M. & Henrissat, B. The
806 carbohydrate-active enzymes database (CAZy) in 2013. *Nucleic Acids Research* **42**, D490–D495
807 (2014).
808 38. Li, D., Wang, J., Liu, Y., Li, Y. & Zhang, Z. Expanded analyses of the functional correlations within
809 structural classifications of glycoside hydrolases. *Computational and Structural Biotechnology*
810 *Journal* **19**, 5931–5942 (2021).
811 39. Gooday, G. W. The ecology of chitin degradation. in *Advances in Microbial Ecology* (ed.
812 Marshall, K. C.) 387–430 (Springer US, Boston, MA, 1990). doi:10.1007/978-1-4684-7612-5_10.
813 40. Morozov, A. A. & Likhoshway, Y. V. Evolutionary history of the chitin synthases of eukaryotes.
814 *Glycobiology* **26**, 635–639 (2016).
815 41. Hamid, R. *et al.* Chitinases: An update. *J Pharm Bioallied Sci* **5**, 21–29 (2013).
816 42. Steinfeld, L., Vafaei, A., Rösner, J. & Merzendorfer, H. Chitin prevalence and function in
817 bacteria, fungi and protists. *Adv Exp Med Biol* **1142**, 19–59 (2019).
818 43. Gerbracht, J. V., Harding, T., Simpson, A. G. B., Roger, A. J. & Hess, S. Comparative
819 transcriptomics reveals the molecular toolkit used by an algivorous protist for cell wall
820 perforation. *Current Biology* **32**, 3374-3384.e5 (2022).
821 44. Zhang, J. *et al.* A receptor required for chitin perception facilitates arbuscular mycorrhizal
822 associations and distinguishes root symbiosis from immunity. *Current Biology* **34**, 1705-1717.e6
823 (2024).
824 45. Malolepszy, A. *et al.* A plant chitinase controls cortical infection thread progression and
825 nitrogen-fixing symbiosis. *eLife* **7**, e38874 (2018).
826 46. Desaki, Y., Miyata, K., Suzuki, M., Shibuya, N. & Kaku, H. Plant immunity and symbiosis signaling
827 mediated by LysM receptors. *Innate Immun* **24**, 92–100 (2018).

828 47. Altura, M. A., Stabb, E., Goldman, W., Apicella, M. & McFall-Ngai, M. J. Attenuation of host NO
829 production by MAMPs potentiates development of the host in the squid-*Vibrio* symbiosis. *Cell*
830 *Microbiol* **13**, 527–537 (2011).
831 48. Aschtgen, M.-S. *et al.* Insights into flagellar function and mechanism from the squid–*Vibrio*
832 symbiosis. *npj Biofilms and Microbiomes* **5**, 1–10 (2019).
833 49. Attah, V. *et al.* Duplication and neofunctionalization of a horizontally transferred xyloglucanase
834 as a facet of the Red Queen coevolutionary dynamic. *Proceedings of the National Academy of*
835 *Sciences* **121**, e2218927121 (2024).
836 50. Hughes, A. L. & Friedman, R. Genome-wide survey for genes horizontally transferred from
837 cellular organisms to baculoviruses. *Molecular Biology and Evolution* **20**, 979–987 (2003).
838 51. Blanc, G. *et al.* The *Chlorella variabilis* NC64A genome reveals adaptation to photosymbiosis,
839 coevolution with viruses, and cryptic sex. *The Plant Cell* **22**, 2943–2955 (2010).
840 52. Richards, T. A. *et al.* Horizontal gene transfer facilitated the evolution of plant parasitic
841 mechanisms in the oomycetes. *Proceedings of the National Academy of Sciences* **108**, 15258–
842 15263 (2011).
843 53. Van Etten, J. L. *et al.* Chloroviruses have a sweet tooth. *Viruses* **9**, E88 (2017).
844 54. Husnik, F. & McCutcheon, J. P. Functional horizontal gene transfer from bacteria to eukaryotes.
845 *Nat. Rev. Microbiol.* **16**, 67–79 (2018).
846 55. Gonçalves, I. R. *et al.* Genome-wide analyses of chitin synthases identify horizontal gene
847 transfers towards bacteria and allow a robust and unifying classification into fungi. *BMC*
848 *Evolutionary Biology* **16**, 252 (2016).
849 56. Savory, F., Leonard, G. & Richards, T. A. The role of horizontal gene transfer in the evolution of
850 the oomycetes. *PLOS Pathogens* **11**, e1004805 (2015).
851 57. Richards, T. A., Hirt, R. P., Williams, B. A. P. & Embley, T. M. Horizontal gene transfer and the
852 evolution of parasitic protozoa. *Protist* **154**, 17–32 (2003).

853 58. Caron, F. & Meyer, E. Does *Paramecium primaurelia* use a different genetic code in its
854 macronucleus? *Nature* **314**, 185–188 (1985).
855 59. Kadono, T., Kawano, T., Hosoya, H. & Kosaka, T. Flow cytometric studies of the host-regulated
856 cell cycle in algae symbiotic with green *Paramecium*. *Protoplasma* **223**, 133–141 (2004).
857 60. Meng, G. *et al.* Structure of human stabilin-1 interacting chitinase-like protein (SI-CLP) reveals a
858 saccharide-binding cleft with lower sugar-binding selectivity. *J Biol Chem* **285**, 39898–39904
859 (2010).
860 61. Kzhyshkowska, J. *et al.* Novel stabilin-1 interacting chitinase-like protein (SI-CLP) is up-
861 regulated in alternatively activated macrophages and secreted via lysosomal pathway. *Blood*
862 **107**, 3221–3228 (2006).
863 62. Xiao, W. *et al.* Human secreted stabilin-1−interacting chitinase-like protein aggravates the
864 inflammation associated with rheumatoid arthritis and is a potential macrophage inflammatory
865 regulator in rodents. *Arthritis & Rheumatology* **66**, 1141–1152 (2014).
866 63. Karunanithi, S. *et al.* Exogenous RNAi mechanisms contribute to transcriptome adaptation by
867 phased siRNA clusters in *Paramecium*. *Nucleic Acids Res* **47**, 8036–8049 (2019).
868 64. Carradec, Q. *et al.* Primary and secondary siRNA synthesis triggered by RNAs from food
869 bacteria in the ciliate *Paramecium tetraurelia*. *Nucleic Acids Res* **43**, 1818–33 (2015).
870 65. Marat, A. L. & Haucke, V. Phosphatidylinositol 3-phosphates—at the interface between cell
871 signalling and membrane traffic. *EMBO J* **35**, 561–579 (2016).
872 66. Raiborg, C., Schink, K. O. & Stenmark, H. Class III phosphatidylinositol 3-kinase and its catalytic
873 product PtdIns3P in regulation of endocytic membrane traffic. *FEBS J* **280**, 2730–2742 (2013).
874 67. Tan, J. X. & Finkel, T. A phosphoinositide signalling pathway mediates rapid lysosomal repair.
875 *Nature* **609**, 815–821 (2022).
876 68. Okkenhaug, K. Signalling by the phosphoinositide 3-kinase family in immune cells. *Annu Rev*
877 *Immunol* **31**, 675–704 (2013).

878 69. O'Donnell, V. B., Rossjohn, J. & Wakelam, M. J. O. Phospholipid signaling in innate immune
879 cells. *J Clin Invest* **128**, 2670–2679.
880 70. Wichterman, R. *The Biology of Paramecium*. (Springer Science & Business Media, 2012).
881 71. Siegel, R. W. Hereditary endosymbiosis in *Paramecium bursaria*. *Exp Cell Res* **19**, 239–52
882 (1960).
883 72. Hollmén, M., Figueiredo, C. R. & Jalkanen, S. New tools to prevent cancer growth and spread: a
884 'Clever' approach. *Br J Cancer* **123**, 501–509 (2020).
885 73. Thumuluri, V., Almagro Armenteros, J. J., Johansen, A. R., Nielsen, H. & Winther, O. DeepLoc
886 2.0: multi-label subcellular localization prediction using protein language models. *Nucleic Acids*
887 *Research* **50**, W228–W234 (2022).
888 74. Doolittle, W. F. You are what you eat: A gene transfer ratchet could account for bacterial genes
889 in eukaryotic nuclear genomes. *Trends Genet.* **14**, 307–311 (1998).
890 75. Howe, C. J., Barbrook, A. C., Nisbet, R. E. R., Lockhart, P. J. & Larkum, A. W. D. The origin of
891 plastids. *Philos Trans R Soc Lond B Biol Sci* **363**, 2675–2685 (2008).
892 76. Larkum, A. W. D., Lockhart, P. J. & Howe, C. J. Shopping for plastids. *Trends Plant Sci* **12**, 189–
893 195 (2007).
894 77. Ricard, G. *et al.* Horizontal gene transfer from bacteria to rumen ciliates indicates adaptation to
895 their anaerobic, carbohydrates-rich environment. *BMC Genomics* **7**, 22 (2006).
896 78. Shaw, F. L. *et al.* Evolution and multifarious horizontal transfer of an alternative biosynthetic
897 pathway for the alternative polyamine sym-homospermidine. *J Biol Chem* **285**, 14711–14723
898 (2010).
899 79. Archibald, J. M. Plastid evolution: Remnant algal genes in ciliates. *Current Biology* **18**, R663–
900 R665 (2008).
901 80. Feng, J.-M. *et al.* Single-cell transcriptome sequencing of rumen ciliates provides insight into
902 their molecular adaptations to the anaerobic and carbohydrate-rich rumen microenvironment.
903 *Molecular Phylogenetics and Evolution* **143**, 106687 (2020).

904 81. Görtz, H.-D. & Fokin, S. I. Diversity of endosymbiotic bacteria in *Paramecium*. in *Endosymbionts*
905 *in Paramecium* (ed. Fujishima, M.) 131–160 (Springer, Berlin, Heidelberg, 2009).
906 doi:10.1007/978-3-540-92677-1_6.
907 82. Flemming, F. E., Grosser, K. & Schrallhammer, M. Natural shifts in endosymbionts' occurrence
908 and relative frequency in their ciliate host population. *Front Microbiol* **12**, 791615 (2022).
909 83. Mironov, T. & Sabaneyeva, E. A robust symbiotic relationship between the ciliate *Paramecium*
910 *multimicronucleatum* and the bacterium ca. *Trichorickettsia Mobilis*. *Frontiers in Microbiology*
911 **11**, (2020).
912 84. Castelli, M. *et al. Deianiraea*, an extracellular bacterium associated with the ciliate
913 *Paramecium*, suggests an alternative scenario for the evolution of *Rickettsiales*. *ISME J* (2019).
914 85. Husnik, F. & Keeling, P. J. The fate of obligate endosymbionts: Reduction, integration, or
915 extinction. *Curr. Opin. Genet. Dev.* **58–59**, 1–8 (2019).
916 86. Husnik, F. & McCutcheon, J. P. Repeated replacement of an intrabacterial symbiont in the
917 tripartite nested mealybug symbiosis. *PNAS* **113**, E5416–E5424 (2016).
918 87. Jacobovitz, M. R. *et al.* Dinoflagellate symbionts escape vomocytosis by host cell immune
919 suppression. *Nat Microbiol* **6**, 769–782 (2021).
920 88. Richter, D. J., Fozouni, P., Eisen, M. B. & King, N. Gene family innovation, conservation and loss
921 on the animal stem lineage. *eLife* **7**, e34226 (2018).
922 89. Woznica, A. *et al.* STING mediates immune responses in the closest living relatives of animals.
923 *eLife* **10**, e70436 (2021).
924 90. Buchmann, K. Evolution of innate immunity: Clues from invertebrates via fish to mammals.
925 *Frontiers in Immunology* **5**, (2014).
926 91. Newman, M.-A., Sundelin, T., Nielsen, J. & Erbs, G. MAMP (microbe-associated molecular
927 pattern) triggered immunity in plants. *Frontiers in Plant Science* **4**, (2013).
928 92. Mogensen, T. H. Pathogen recognition and inflammatory signaling in innate immune defenses.
929 *Clin Microbiol Rev* **22**, 240–273 (2009).

930 93. Flemming, F. E., Potekhin, A., Pröschold, T. & Schrallhammer, M. Algal diversity in *Paramecium*
931 *bursaria*: Species identification, detection of *Choricystis parasitica*, and assessment of the
932 interaction specificity. *Diversity* **12**, 287 (2020).
933 94. Douglas, A. E. Conflict, cheats and the persistence of symbioses. *New Phytologist* **177**, 849–858
934 (2008).
935 95. Ågren, J. A., Davies, N. G. & Foster, K. R. Enforcement is central to the evolution of
936 cooperation. *Nat Ecol Evol* **3**, 1018–1029 (2019).
937 96. Spanner, C., Darienko, T., Filker, S., Sonntag, B. & Pröschold, T. Morphological diversity and
938 molecular phylogeny of five *Paramecium bursaria* (Alveolata, Ciliophora, Oligohymenophorea)
939 syngens and the identification of their green algal endosymbionts. *Sci Rep* **12**, 18089 (2022).
940 97. Spragge, F. *et al.* Microbiome diversity protects against pathogens by nutrient blocking. *Science*
941 (2023) doi:10.1126/science.adj3502.
942 98. Irwin, N. A. T., Pittis, A. A., Richards, T. A. & Keeling, P. J. Systematic evaluation of horizontal
943 gene transfer between eukaryotes and viruses. *Nat Microbiol* **7**, 327–336 (2022).
944 99. Katoh, K. & Standley, D. M. MAFFT multiple sequence alignment software version 7:
945 Improvements in performance and usability. *Molecular Biology and Evolution* **30**, 772–780
946 (2013).
947 100. Capella-Gutiérrez, S., Silla-Martínez, J. M. & Gabaldón, T. trimAl: A tool for automated
948 alignment trimming in large-scale phylogenetic analyses. *Bioinformatics* **25**, 1972–1973 (2009).
949 101. Nguyen, L.-T., Schmidt, H. A., von Haeseler, A. & Minh, B. Q. IQ-TREE: A fast and effective
950 stochastic algorithm for estimating maximum-likelihood phylogenies. *Mol Biol Evol* **32**, 268–
951 274 (2015).
952 102. Irwin, N. A. T. *et al.* The function and evolution of motile DNA replication systems in ciliates.
953 *Current Biology* (2020) doi:10.1016/j.cub.2020.09.077.
954 103. Bates, D., Mächler, M., Bolker, B. & Walker, S. Fitting linear mixed-effects models using lme4.
955 *Journal of Statistical Software* **67**, 1–48 (2015).

956 104. Kuznetsova, A., Brockhoff, P. B. & Christensen, R. H. B. lmerTest package: Tests in linear mixed
957 effects models. *Journal of Statistical Software* **82**, 1–26 (2017).
958 105. Martin, M. Cutadapt removes adapter sequences from high-throughput sequencing reads.
959 *EMBnet.journal* **17**, 10–12 (2011).
960 106. Langmead, B. & Salzberg, S. L. Fast gapped-read alignment with Bowtie 2. *Nat Methods* **9**, 357–
961 359 (2012).
962 107. Li, H. *et al.* The sequence alignment/map format and SAMtools. *Bioinformatics* **25**, 2078–2079
963 (2009).
964 108. Patro, R., Duggal, G., Love, M. I., Irizarry, R. A. & Kingsford, C. Salmon provides fast and bias-
965 aware quantification of transcript expression. *Nat Methods* **14**, 417–419 (2017).
966 109. Love, M. I., Huber, W. & Anders, S. Moderated estimation of fold change and dispersion for
967 RNA-seq data with DESeq2. *Genome Biology* **15**, 550 (2014).
968 110. Pang, Z. *et al.* MetaboAnalyst 5.0: Narrowing the gap between raw spectra and functional
969 insights. *Nucleic Acids Research* **49**, W388–W396 (2021).
970 111. Benjamini, Y. & Hochberg, Y. Controlling the false discovery rate: A practical and powerful
971 approach to multiple testing. *Journal of the Royal Statistical Society: Series B (Methodological)*
972 **57**, 289–300 (1995).
973 112. Kaever, A. *et al.* MarVis: A tool for clustering and visualization of metabolic biomarkers. *BMC*
974 *Bioinformatics* **10**, 92 (2009).
975 113. Kanehisa, M., Sato, Y., Furumichi, M., Morishima, K. & Tanabe, M. New approach for
976 understanding genome variations in KEGG. *Nucleic Acids Research* **47**, D590–D595 (2019).
977 114. Caspi, R. *et al.* The MetaCyc database of metabolic pathways and enzymes. *Nucleic Acids*
978 *Research* **46**, D633–D639 (2018).
979 115. Rueden, C. T. *et al.* ImageJ2: ImageJ for the next generation of scientific image data. *BMC*
980 *Bioinformatics* **18**, 529 (2017).
981

982 **Figures**

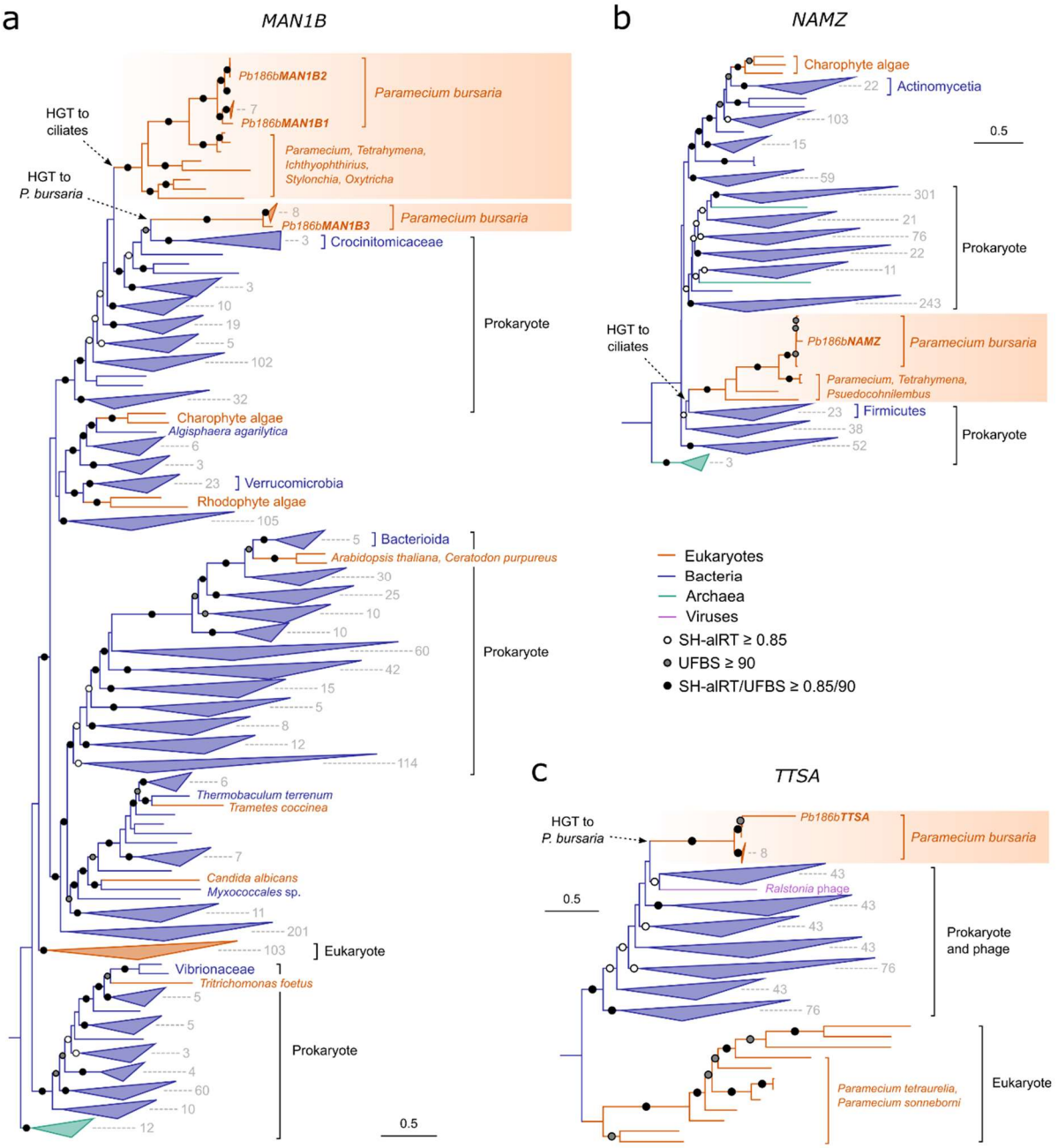

983

984 **Figure 1: Horizontal gene-transfer has shaped glycan-processing in *P. bursaria*.** Maximum likelihood phylogenies of *Pb β-*
985 *mannosidase* (*MAN1B*; ***a***), *NamZ-like lysozyme* (*NAMZ*; ***b***), and *TtsA-like lysozyme* (*TTSA*; ***c***) genes. Topologies of these trees
986 provide strong support for prokaryote-to-eukaryote HGT, with two independent incidences of HGT and a subsequent gene
987 duplication of *MAN1B1/2* predicted to have occurred in *Pb* (***a***). We observed no evidence of *MAN1B2* transcription
988 (**Supplementary Table S1**) indicating possible pseudogenization of *MAN1B2* in *Pb* 186b. Trees were generated in IQ-TREE
989 using Q.pfam+R10 (***a***), Q.pfam+I+R10 (***b***), or Q.pfam+R7 (***c***) substitution models selected by Model Finder, and statistical
990 support assessed using SH-aLRT and ultra-fast bootstraps (UFBS; *n* = 1000). This figure shows four cases of HGT of GH gene
991 families, for phylogenies of four additional predicted HGT-derived GH encoding genes in *Pb* see **Fig. S2.**

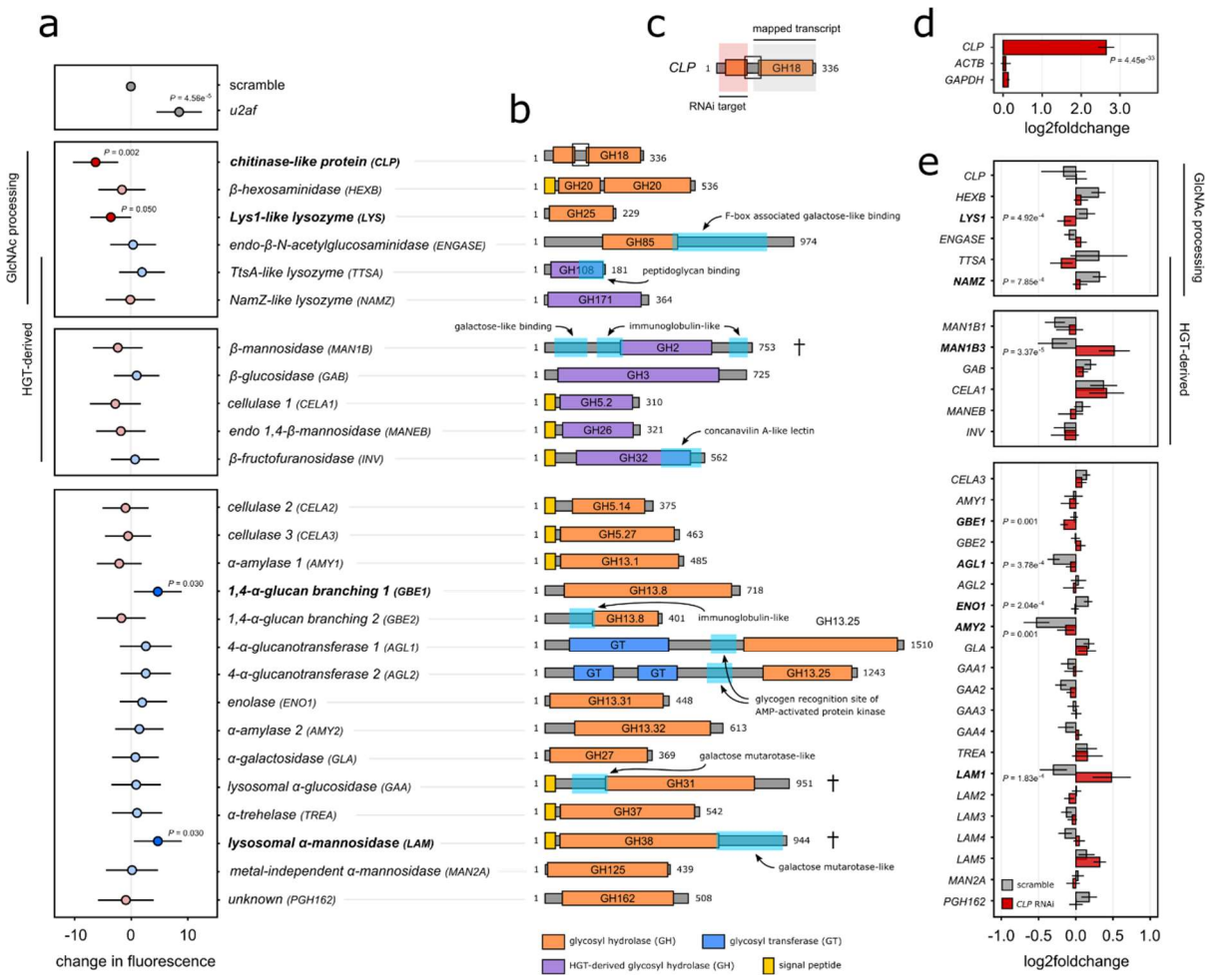

992

993 **Figure 2: RNAi of a subset of glycan-processing genes perturbs host-mediated endosymbiont destruction, and perturbation**
994 **of *CLP* determines expression of glycan-processing genes.** All experiments were conducted using *Pb* cultures containing 75-
995 100 cells (***a***) or 250,000 (***d, e***) cells. Cultures were fed daily with HT115 *E. coli* expressing target dsRNA to induce RNAi, or a
996 non-hit 'scramble' dsRNA control. Per-host fluorescence is used throughout as a proxy for endosymbiotic algal load. ***a***, Change
997 in per host fluorescence, compared to scramble treatment, in RNAi treated *Pb* cultures (n = 12) during endosymbiont break-
998 down. Cells were fed under standard conditions for 4 days, followed by 2 days of simultaneous RNAi feeding and
999 cycloheximide treatment (50 μgmL^{-1}) to trigger endosymbiont digestion. ***b***, Schematic illustration of functional domain
1000 architecture of host putative glycosyl hydrolase (GH) encoding genes. For chimeric constructs (†) targeting multiple genes a
1001 single representative is shown (see **Fig. S3** for all genes). GH, glycosyl hydrolase (orange/purple); GT, glycosyl transferase
1002 (blue); additional domains are highlighted in cyan. ***c***, Schematic illustration of *CLP* RNAi construct design including dsRNA
1003 target (red) and mapped transcript region for differential expression analysis (grey). ***d***, Change in *CLP* gene expression (***c***)
1004 during RNAi treatment in untreated cultures, compared to Actin and GAPDH housekeeping genes. ***e***, Change in GH transcript
1005 expression in scramble (grey) or *CLP* RNAi treated (red) *Pb* cultures (n = 6) during cycloheximide induced endosymbiont break-
1006 down, compared to respective scramble or *CLP* RNAi cultures without cycloheximide treatment (see also **Supplementary**
1007 **Table S2**). Statistical significance is shown for difference in log2foldchange values between scramble and *CLP* RNAi conditions.
1008 For all data, statistical significance was calculated using a linear mixed effects model (***a***) or an un-paired two-tailed t-test (***d***,
1009 ***e***)**.** Conditions where (***a***) $p < 0.05$ or (***e***) Bonferroni-corrected $p < 0.0015$ are shown.

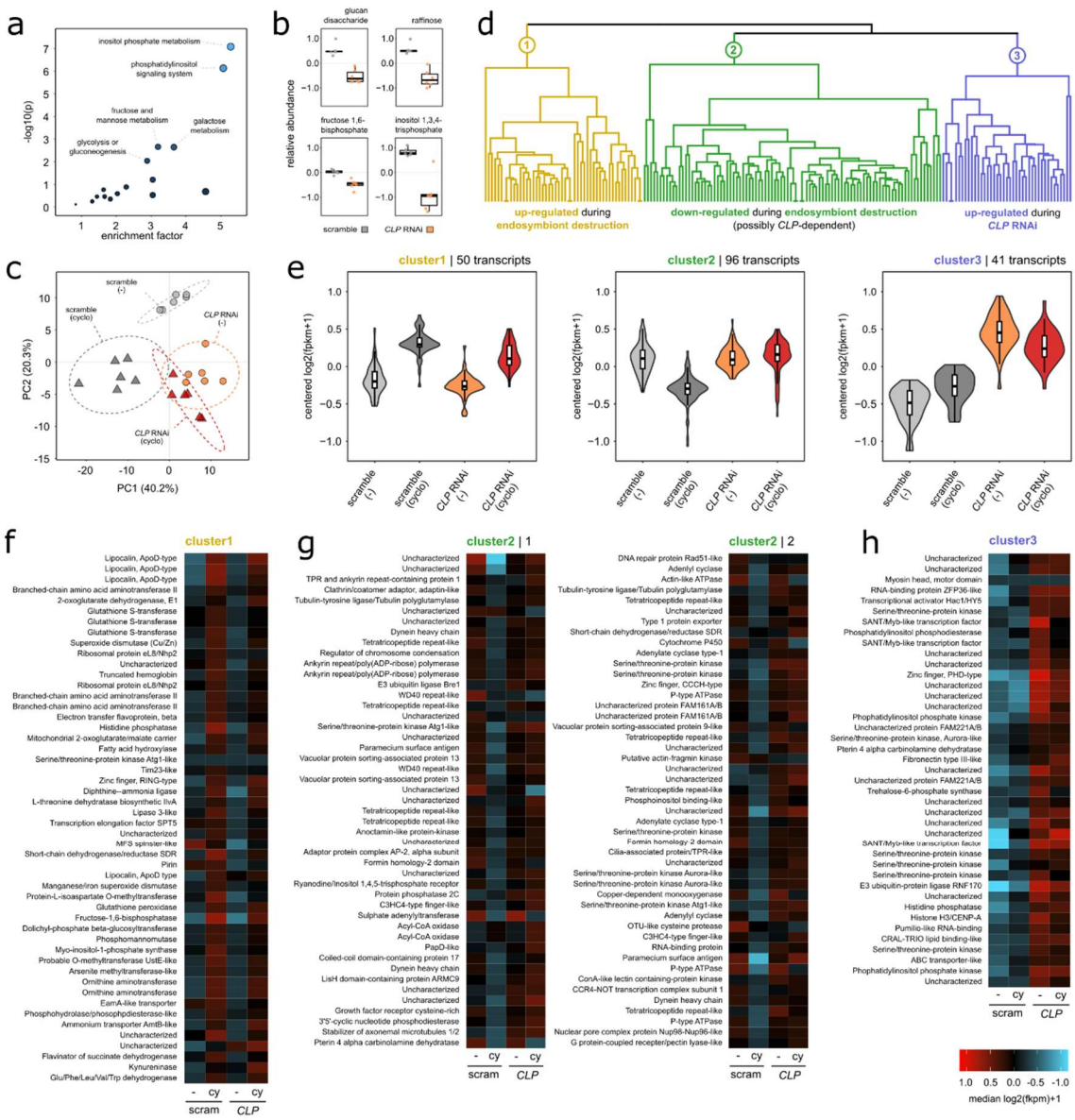

Figure 3: *CLP* RNAi alters expression of transcription factors and intracellular signalling systems. All experiments were conducted using *Pb* cultures (*n* = 6) containing approximately 250,000 cells. Cultures were fed daily with HT115 *E. coli* expressing target dsRNA to induce *CLP* knock-down, or 'scramble' dsRNA control with no hits to sampled *Pb* genes. ***a,*** Enrichment plot of significantly altered pathways during *CLP* RNAi, compared to a scramble control, detected by untargeted metabolomics (see also **Supplementary Table S3**). ***b,*** Relative abundance of significantly altered metabolites detected during *CLP* RNAi. ***c,*** PCA plot showing variance of transcriptional profiles in *Pb* cultures during *CLP* RNAi (orange, red) compared to a scramble control (grey, dark grey). Samples were treated with 50 µgmL^{-1} cycloheximide (triangle; cyclo) to trigger endosymbiont break-down, or remained untreated (circle; -). The percentage of explained variance for each PC is displayed. ***d,*** Hierarchical clustering of differentially expressed transcripts ([log2 fold change] ≥ 1, adjusted p value < 0.001) in each pairwise comparison. Clusters were defined through a dendogram maximum height cut-off of 80%. ***e,*** Three clusters of transcripts with similar expression patterns resulting from the cut dendogram (see also **Supplementary Table S4**) Data represented as median values (*n* = 6) of all transcripts from each cluster with overlaid distribution density. ***f-h,*** Heatmap of read-centred expression in each sample condition, and transcript annotation (InterProScan), for each of the identified transcript clusters. For relative abundance of all identified significantly altered metabolites during *CLP* RNAi, see **Fig. S4**. For individual heatmaps of each pairwise comparison across replicates during differential expression analysis, see **Fig. S6**.

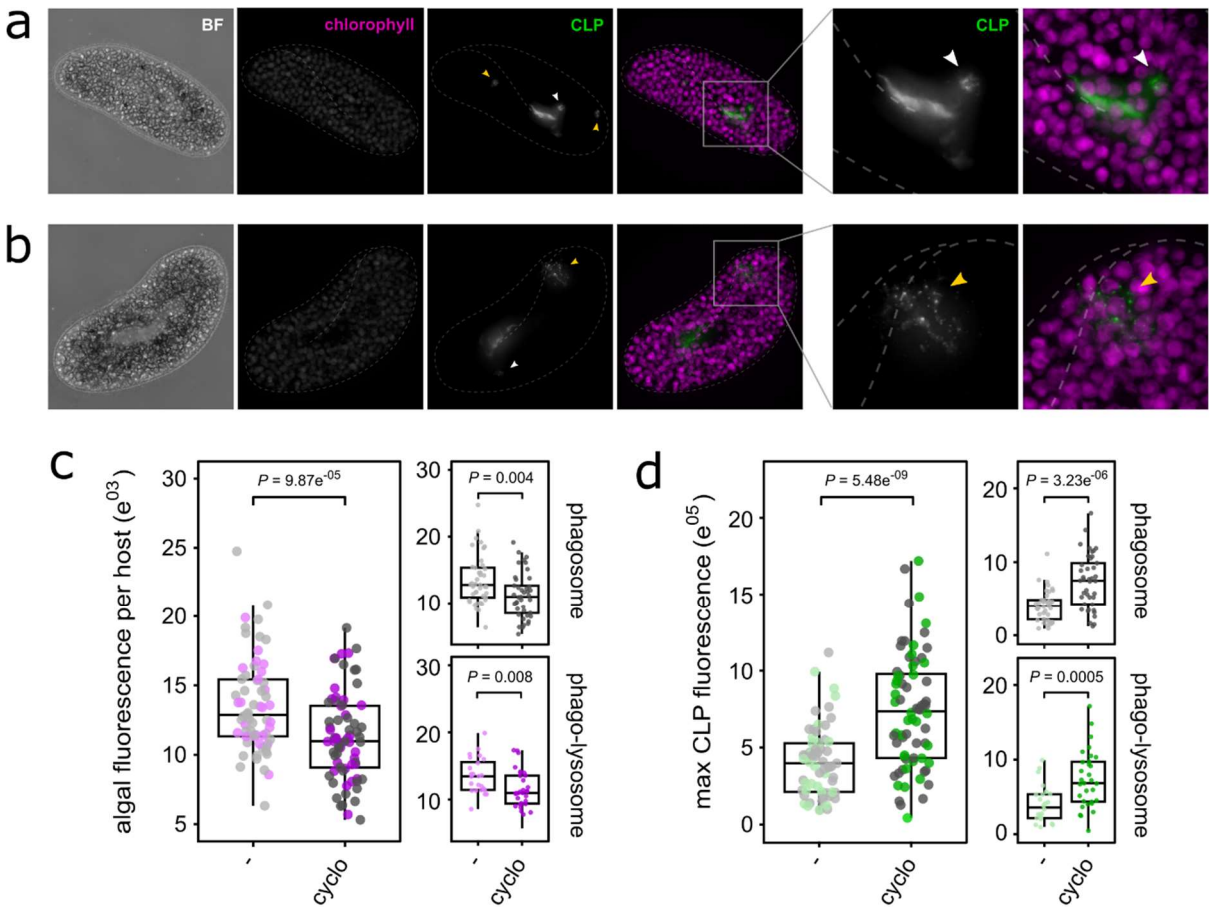

Figure 4: CLP localizes proximate to the putative host phagosome and lysosome during endosymbiont destruction. All experiments were conducted using *Pb* cells grown under standard conditions (- ; *n* = 70), or treated with 50 µgmL^{-1} cycloheximide (cyclo ; *n* = 69). All cells were treated a primary αCLP antibody followed by an Alexa Fluor 488-conjugated secondary antibody for immunofluorescence imaging. ***a-b***, Fluorescence imaging of *Pb* cells exhibiting phagosome-like (***a*** ; white arrows) or lysosome-like (***b*** ; yellow arrows) CLP localization. Magenta indicates endosymbiotic algal autofluorescence, green indicates Alexa Fluor 488 secondary antibody fluorescence. ***c-d*** Mean algal fluorescence (***c***) and max CLP fluorescence (***d***) per host cell in untreated (-) or cycloheximide treated (cyclo) cells. Cells were scored based on whether they exhibited phagosome- or phagosome/lysosome-like *CLP* localization. Boxplot data are represented as max, upper quartile (Q3), mean, lower quartile (Q1) and min values, and individual data points for each biological replicate are shown. Statistical significance was calculated using a linear model.

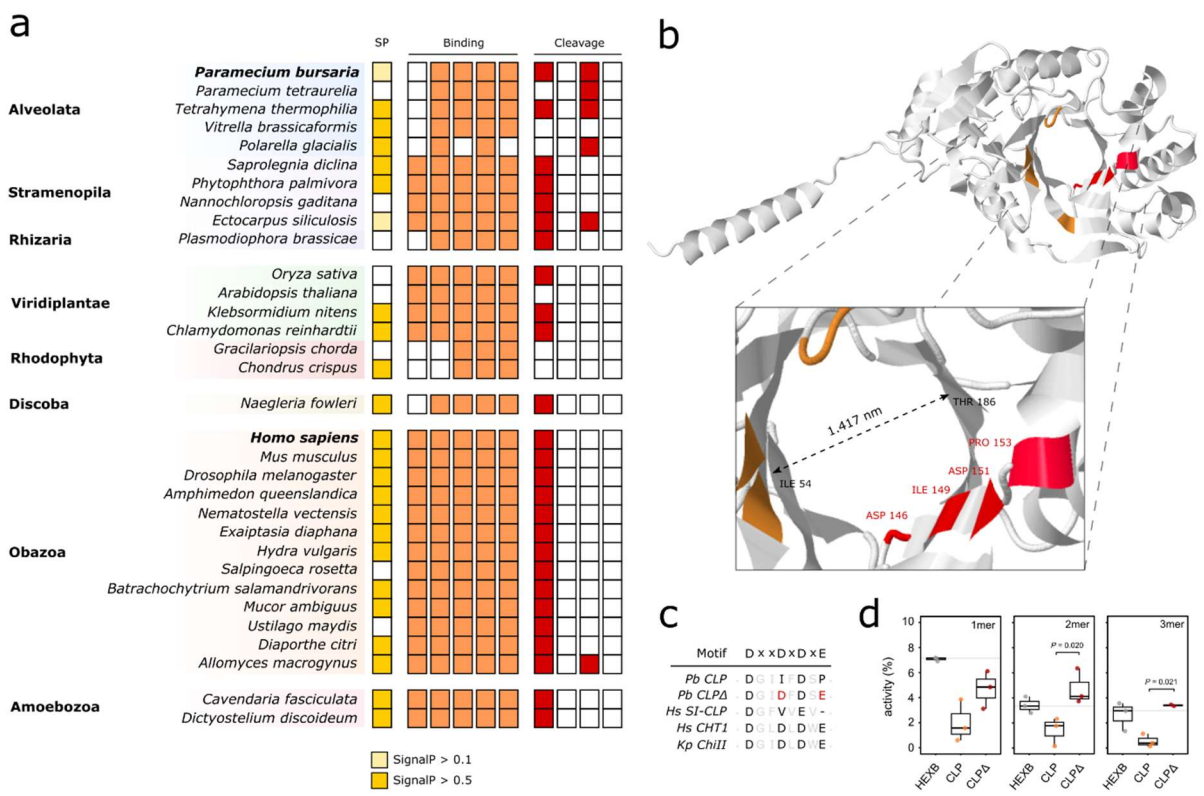

Figure 5: CLP is a chitin-binding protein homologous to an animal immune factor. a, Conserved functional domain residues of *CLP* across a sample of eukaryotic protein homologues (see also **Fig. S7**) including predicted signal peptide (yellow) and characterised binding (orange) and cleavage (red) site amino acids. ***b,*** Predicted 3D structure of *Pb* CLP generated with AlphaFold3 (see also **Fig. S8**). Characterised binding (orange) and cleavage sites (red) are highlighted. ***c,*** Trimmed amino acid alignment of *Pb CLP* and *Hs SI-CLP* sequences, compared to known chitin-cleaving enzymes *Hs CHT1* and *K. pneumoniae ChiII*. Residues in bold are sites associated with a conserved chitin-cleavage motif. Residues in red indicate synthetically mutated sites to 'restore' chitin-cleaving function. ***d.*** Percentage activity of purified wild-type (CLP) and mutated (CLPΔ) *Pb* enzymes incubated for 3 hours in 1mer (GlcNAc), 2mer ($GlcNAc_2$; $Chitin_2$), or 3mer ($GlcNAc_3$; $Chitin_3$) chitin substrates. Enzymes were synthesized to encode a 5' yeast secretion signal, transformed into chitinase-deficient *Saccharomyces cerevisiae* strain Y16947, and expressed under selection for 7 days. Supernatant containing the expressed enzyme was concentrated, washed, and protein concentrations matched prior to the assay. Activity was standardised against supernatant from a yeast empty vector control. *Pb β-hexosaminidase* (**Fig. 2b**), an enzyme predicted to cleave terminal GlcNAc residues from glycan chains, was used as a positive control (HEXB). Boxplot data are represented as max, upper quartile (Q3), mean, lower quartile (Q1) and min values, and individual data points for each biological replicate are shown. Statistical significance was calculated using generalized linear models with quasi-binomial error distribution.

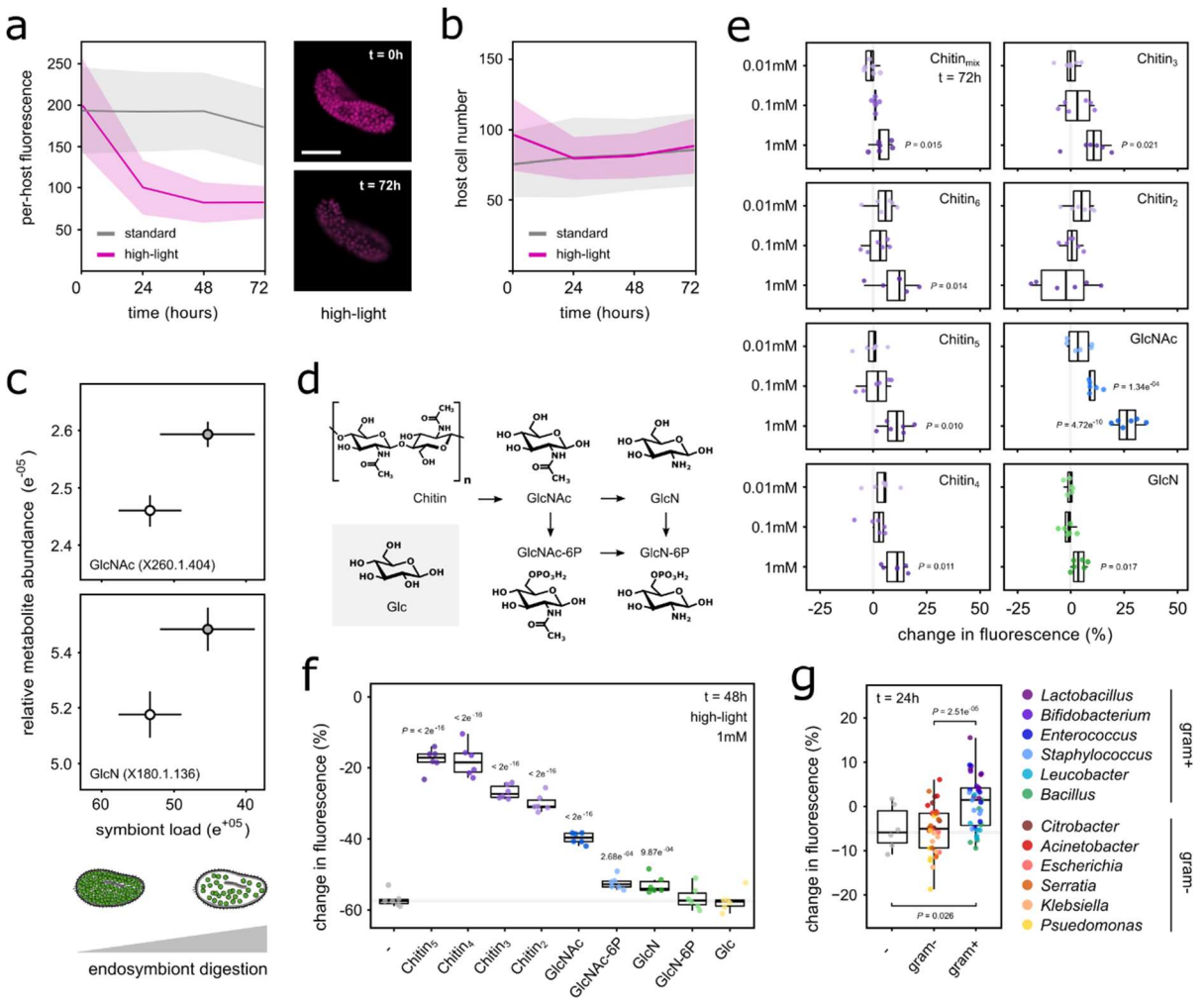

Figure 6: Glycan break-down products alter host control of endosymbiotic algae. All experiments were conducted using pre-starved *Pb* cultures (n = 6) grown under standard conditions (see **Methods**), unless stated otherwise. Growth under standard light was conducted at 25 µ mol m^{-2} s^{-1}, high-light at 80 µ mol m^{-2} s^{-1}, moderate high-light at 50 µ mol m^{-2} s^{-1}, and low-light at 6 µ mol m^{-2} s^{-1}. Per host fluorescence is used throughout as a proxy for endosymbiotic algal load. ***a***, Mean per host fluorescence in *Pb* cultures grown under high-light. Data are presented as mean ± sd. Scale bar = 50µm, magenta indicates endosymbiotic algal autofluorescence. ***b***, Host cell number in *Pb* cultures grown under high-light for 72 hours. Data are presented as mean ± sd. ***c***, Relative metabolite abundance in *Pb* cultures under variant light conditions, in which differential endosymbiont digestion is known to occur. Cells were grown under moderate high-light (white) or low-light (grey) for 3 days prior to metabolite extraction, and symbiont load per host-cell assessed by flow cytometry (**Fig. S10**). ***d***, Schematic metabolic pathway of chitin break-down, including the structure of glucose (Glc) for comparison. ***e***, Percentage change in per host fluorescence following exposure to chitin and chitin break-down products, compared to an untreated control. Cells were exposed to chitin (mixed oligosaccharides, or oligosaccharide lengths 6 to 2), GlcNAc, or GlcN for 72 hours. ***f***, Percentage change in per host fluorescence upon exposure to chitin break-down products during high-light initiated endosymbiont digestion. Cells were grown under high-light and exposed to chitin (oligosaccharide length 5 to 2), chitin break-down products (see ***d***), or Glc for 48 hours. Each substrate was added to a final concentration of 1mM. ***g***, Pooled percentage change in per host fluorescence following bacterial feeding in standard growth conditions. *Pb* cells were grown for 24 hours, and bacteria were heat-killed and matched to OD 0.1 prior to feeding (**Fig. S12**). All boxplot data are represented as max, upper quartile (Q3), mean, lower quartile (Q1) and min values, and individual data points for each biological replicate are shown. Statistical significance was calculated using a linear model on log-transformed data (**e**, **f**, **g**). Conditions where $p < 0.05$ are shown.

1073 GlcNAc, N-acetyl-D-glucosamine; GlcN, D-glucosamine; GlcNAc-6P, N-acetyl-D-glucosamine-6-phosphate; GlcN-6P, D-
1074 glucosamine-6-phosphate; Glc, Glucose.